N-(4-Hydroxyphenyl) Retinamide Suppresses SARS-CoV-2 Spike Protein-Mediated Cell-Cell Fusion by a Dihydroceramide Δ4-Desaturase 1-Independent Mechanism

Yasuhiro Hayashi,[a] Kiyoto Tsuchiya,[b] Mizuki Yamamoto,[c] Yoko Nemoto-Sasaki,[a] Kazunari Tanigawa,[a] Kotaro Hama,[a] Yusuke Ueda,[a] Takashi Tanikawa,[d] Jin Gohda,[c] Kenji Maeda,[e] Jun-ichiro Inoue,[f] Atsushi Yamashita[a]

aFaculty of Pharma-Science, Teikyo University, Tokyo, Japan
bAIDS Clinical Center, National Center for Global Health and Medicine Hospital, Tokyo, Japan
cResearch Center for Asian Infectious Diseases, The Institute of Medical Science, The University of Tokyo, Tokyo, Japan
dFaculty of Pharmacy and Pharmaceutical Sciences, Josai University, Saitama, Japan
eDepartment of Refractory Viral Infections, National Center for Global Health and Medicine Research Institute, Tokyo, Japan
fSenior Professor Office, The University of Tokyo, Tokyo, Japan

ABSTRACT The membrane fusion between the severe acute respiratory syndrome coronavirus 2 (SARS-CoV-2) and host cells is essential for the initial step of infection; therefore, the host cell membrane components, including sphingolipids, influence the viral infection. We assessed several inhibitors of the enzymes pertaining to sphingolipid metabolism, against SARS-CoV-2 spike protein (S)-mediated cell-cell fusion and viral infection. N-(4-Hydroxyphenyl) retinamide (4-HPR), an inhibitor of dihydroceramide Δ4-desaturase 1 (DES1), suppressed cell-cell fusion and viral infection. The analysis of sphingolipid levels revealed that the inhibition efficiencies of cell-cell fusion and viral infection in 4-HPR-treated cells were consistent with an increased ratio of saturated sphinganine-based lipids to total sphingolipids. We investigated the relationship of DES1 with the inhibition efficiencies of cell-cell fusion. The changes in the sphingolipid profile induced by 4-HPR were mitigated by the supplementation with exogenous cell-permeative ceramide; however, the reduced cell-cell fusion could not be reversed. The efficiency of cell-cell fusion in DES1 knockout (KO) cells was at a level comparable to that in wild-type (WT) cells; however, the ratio of saturated sphinganine-based lipids to the total sphingolipids was higher in DES1 KO cells than in WT cells. 4-HPR reduced cell membrane fluidity without any significant effects on the expression or localization of angiotensin-converting enzyme 2, the SARS-CoV-2 receptor. Therefore, 4-HPR suppresses SARS-CoV-2 S-mediated membrane fusion through a DES1-independent mechanism, and this decrease in membrane fluidity induced by 4-HPR could be the major cause for the inhibition of SARS-CoV-2 infection.

IMPORTANCE Sphingolipids could play an important role in SARS-CoV-2 S-mediated membrane fusion with host cells. We studied the cell-cell fusion using SARS-CoV-2 S-expressing cells and sphingolipid-manipulated target cells, with an inhibitor of the sphingolipid metabolism. 4-HPR (also known as fenretinide) is an inhibitor of DES1, and it exhibits antitumor activity and suppresses cell-cell fusion and viral infection. 4-HPR suppresses membrane fusion through a decrease in membrane fluidity, which could possibly be the cause for the inhibition of SARS-CoV-2 infection. There is accumulating clinical data on the safety of 4-HPR. Therefore, it could be a potential candidate drug against COVID-19.

KEYWORDS SARS-CoV-2, antiviral agents, sphingolipid

The coronavirus disease (COVID-19) pandemic, caused by severe acute respiratory syndrome coronavirus 2 (SARS-CoV-2), originates from Wuhan, Hubei Province,

L-Serine + Palmitoyl-CoA

SPT ⊣ myriocin

3-Ketodihydrosphingosine

dihydrosphingosine

CerS ⊣ fumonisin B1

sphinganine-based lipids

dihydroceramide (DHCer)

dihydroglucosylceramide (DHGlcCer) ← *GCS* — dihydrosphingomyelin (DHSM) *CERT* →

threo-PPMP

DES1 ⊣ 4-HPR, GT11   HPA12

sphingosine-based lipids

Ceramide (Cer)

Glucosylceramide (GlcCer) ← *GCS* / *GBA1* → Sphingomyelin (SM) *CERT* / *SMase*

CBE

GW4869, amitriptyline

CDase ⊣ ceranib-2

Sphingosine (SPH)

SKase ⊣ SKI-II

Sphingosine-1-Phosphate (S1P)

⊣ FTY720

signalling via S1P receptors

FIG 1 Enzymes involved in the sphingolipid metabolic pathway and their inhibitors in mammalian cells. The enzymes and inhibitors analyzed in this study are shown in blue and red, respectively. DHCer, DHGlcCer, and DHSM are composed of a saturated sphingoid base backbone sphinganine and a fatty acid of varying length. Cer, GlcCer, and SM are composed of an unsaturated sphingoid base backbone sphingosine and a fatty acid varying in length. In mammalian cells, DHCer is desaturated by DES1, generating a 4,5-*trans*-double bond to form Cer.

China (1–4). As of the end of May 2021, more than 160 million people have been infected worldwide, with more than 3 million deaths in 220 countries (https://www.worldometers.info/coronavirus/). Although the pandemic wave of COVID-19 continues, therapeutic options remain limited.

Sphingolipids are critical to all stages of the viral life cycle, such as the binding in human rhinovirus (5), entry in influenza virus (6), replication in hepatitis C virus (7), and cell lysis and release in adenovirus (8). We found that sphingomyelin synthase 2, involved in the synthesis of sphingomyelin (SM), can promote HIV-1 envelope-mediated membrane fusion (9). Recently, Vitner et al. (10) reported that the glucosylceramide synthase (GCS) inhibitors Genz-123346 and Genz-667161 block the infection of RNA viruses, including the neuroinvasive Sindbis virus, West Nile virus, influenza A virus, and SARS-CoV-2. This study suggested that sphingolipids are involved in SARS-CoV-2 infection; however, the lipid profiles of inhibitor-treated cells were not examined. Therefore, the precise function of sphingolipids in SARS-CoV-2 infection remains unclear.

Sphingolipid metabolism involves a dynamic network of molecules, including important bioactive signaling molecules (Fig. 1) (11, 12). *De novo* biosynthesis of sphingolipids occurs in the endoplasmic reticulum and begins with the condensation of
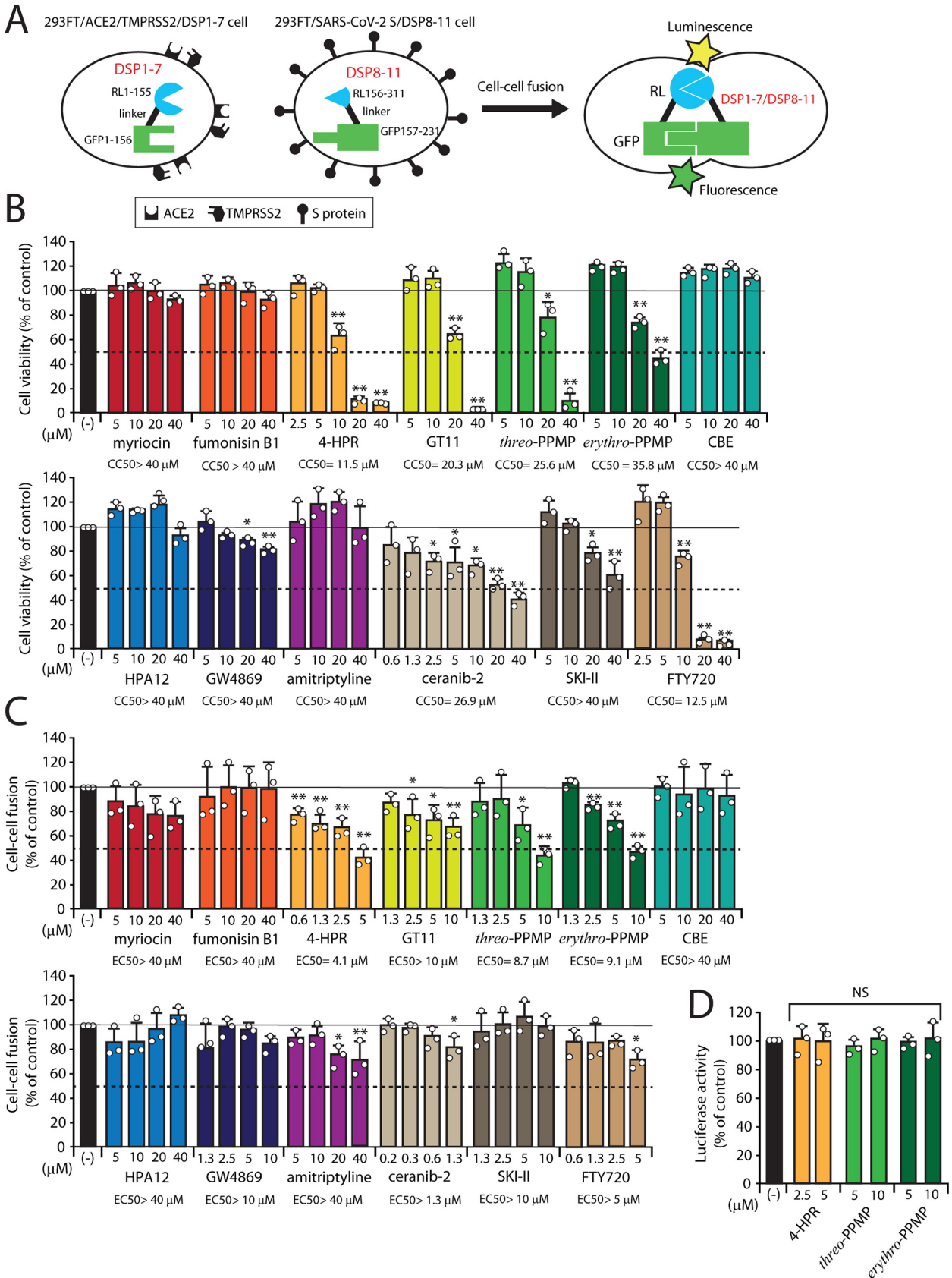
FIG 2 Effect of inhibitors of sphingolipid-metabolizing enzymes on SARS-CoV-2 S protein-mediated membrane fusion, as examined by DSP-based cell-cell fusion assay. The effects of compounds on cell viability and cell-cell fusion were examined in 293FT/ACE2/TMPRSS2/DSP1-7 cells

(Continued on next page)

TABLE 1 Effects of the 13 compounds against the SARS-CoV-2 S protein-mediated cell-cell fusion at nontoxic concentrations of each compound

Inhibitor	CC_{50} (μM)	EC_{50} (μM)
Myriocin	>40	>40
Fumonisin B1	>40	>40
4-HPR	11.5	4.1
GT11	20.3	>10
threo-PPMP	25.6	8.7
erythro-PPMP	35.8	9.1
CBE	>40	>40
HPA12	>40	>40
GW4869	>40	>10
Amitriptyline	>40	>40
Ceranib-2	26.9	>1.3
SKI-II	>40	>10
FTY720	12.5	>5

L-serine with palmitoyl coenzyme A (CoA) to produce 3-ketodihydrosphingosine in a reaction catalyzed by serine palmitoyltransferase (SPT). 3-Ketodihydrosphingosine is reduced to dihydrosphingosine, which is *N*-acylated to dihydroceramide (DHCer) by ceramide synthase (CerS). The length of the *N*-acyl chain in DHCer is determined by the specificity of different CerSs; $C_{16:0}$, $C_{18:0}$, $C_{24:0}$, and $C_{24:1}$ are the major fatty acids incorporated into DHCer in mammalian cells (13). The formation of ceramide (Cer), the core structure of sphingolipids, involves insertion of a single double bond into DHCer by dihydroceramide Δ4-desaturase 1 (DES1). Cer, and to a lesser extent DHCer, is further metabolized to form complex sphingolipids, such as sphingomyelins (SM and DHSM, respectively) and glucosylceramides (GlcCer and DHGlcCer, respectively) in the Golgi apparatus. DHCer, DHSM, and DHGlcCer are composed of saturated sphingoid base backbones (sphinganine), while Cer, SM, and GlcCer are composed of unsaturated sphingoid base backbones (sphingosine [Sph]). Most of the genes encoding sphingolipid-metabolizing enzymes, as well as several inhibitors of sphingolipid-metabolizing enzymes, have been identified (14–24).

SARS-CoV-2 must penetrate the cell membrane to infect cells. Therefore, in the present study, we tested the ability of inhibitors against the enzymes of the sphingolipid metabolism, for altering the membrane environment, making the virus penetration difficult, and subsequently preventing infection. To understand the function of sphingolipids in SARS-CoV-2 infection, we analyzed the quantitative sphingolipid metabolome of the inhibitor-treated cells using liquid chromatography-tandem mass spectrometry (LC-MS/MS).

RESULTS

4-HPR inhibits SARS-CoV-2 spike (S) protein-mediated cell-cell fusion. Membrane fusion between SARS-CoV-2 and host cells is essential for the early step of the infection, and therefore, the membrane composition, including that of sphingolipids, in host cells could influence the viral infection. To investigate the roles of sphingolipids in

FIG 2 Legend (Continued)

treated for 2 days with the indicated concentrations of the compounds. (A) The structures of DSP1-7 and DSP8-11 are *Renilla* luciferase (RL)1-155-glycine linker-green fluorescent protein (GFP)1-156 and Met-RL156-311-glycine linker-GFP157-231, respectively. DSP1-7 and DSP8-11 reassociate efficiently, resulting in reconstitution of a functional RL and GFP to generate luminescent and fluorescent signals, respectively. (B) Cell viability was examined using the WST-8 [2-(2-methoxy-4-nitrophenyl)-3-(4-nitrophenyl)-5-(2, 4-disulfophenyl)-2H-tetrazolium, monosodium salt] assay. Results are normalized to the rate of cell viability in vehicle/DMSO-treated cells. (C) The susceptibility of cell-cell fusion was examined using the DSP-based cell-cell fusion assay. Results are normalized to the rate of cell-cell fusion in vehicle/DMSO-treated cells. (D) HEK293FT cells expressing DSP1-7 and DSP8-11 were treated for 2 days with the indicated concentrations of the compounds, and then RL activity was measured. Results are normalized to the rate of cell-cell fusion in vehicle/DMSO-treated cells. Values represent the mean $\pm$ SD from three independent experiments. Statistical significance was determined using one-way ANOVA followed by Dunnett test for multiple comparisons; *, $P < 0.05$; **, $P < 0.01$ versus vehicle/DMSO-treated cells; NS, not significant. CC_{50} and EC_{50} values were determined using GraphPad Prism 6 software. Individual data points are shown as a scatterplot.
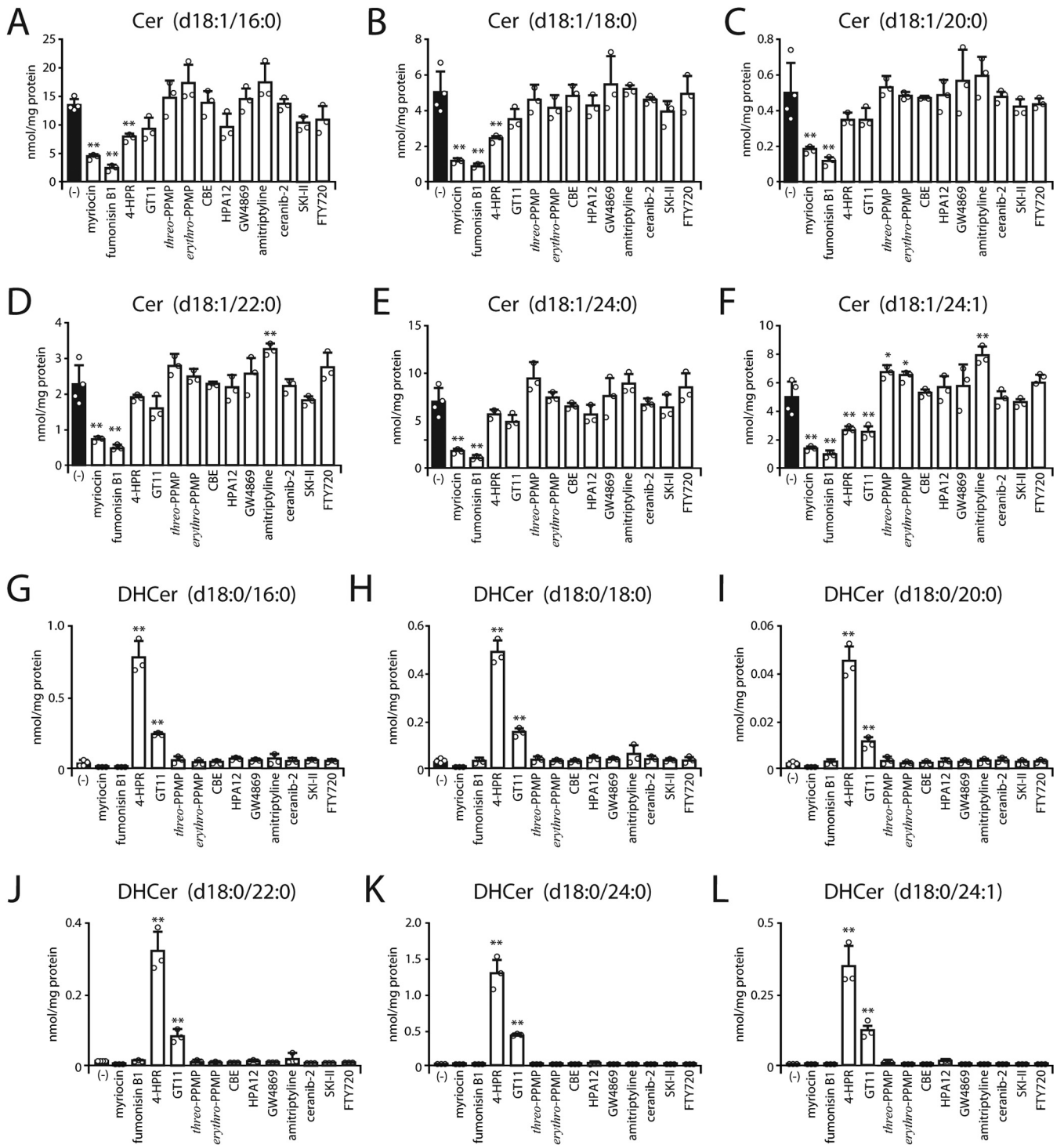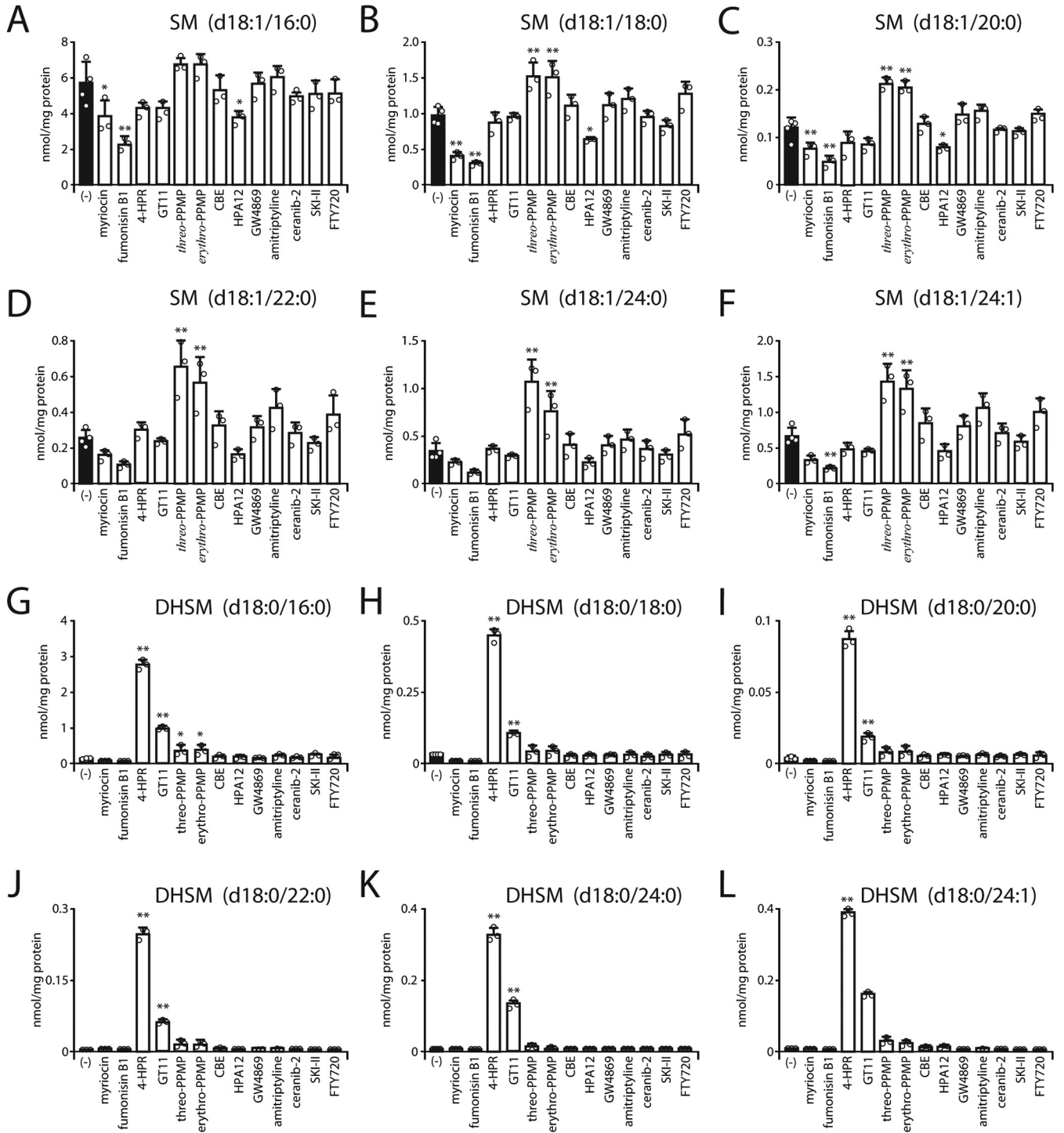
FIG 3 Effect of sphingolipid-metabolizing enzyme inhibitors on cellular Cer and DHCer species in 293FT/ACE2/TMPRSS2/DSP1-7 cells. 293FT/ACE2/TMPRSS2/DSP1-7 cells were treated for 2 days with each of the compounds as follows: 40 μM myriocin, 40 μM fumonisin B1, 5 μM 4-HPR, 10 μM GT11, 10 μM *threo*-PPMP, 10 μM *erythro*-PPMP, 40 μM CBE, 40 μM HPA12, 10 μM GW4869, 40 μM amitriptyline, 1.3 μM ceranib-2, 10 μM SKI-II, and 5 μM FTY720. The cellular levels of Cer and DHCer species with a distinct acyl chain were quantified using LC-MS/MS. The bar graphs show levels of Cer (A to F) and DHCer (G to L). Statistical significance was determined using one-way ANOVA followed by Dunnett test for multiple comparisons; *, $P < 0.05$; **, $P < 0.01$ versus vehicle/DMSO-treated cells. Individual data points are shown as a scatterplot.

SARS-CoV-2 S protein-mediated membrane fusion, we employed the dual split protein (DSP)-based cell-cell fusion assay using SARS-CoV-2-mimicking cells and sphingolipid-manipulated target cells treated with an inhibitor of an enzyme functioning in the sphingolipid metabolism. The membrane fusion efficiency between 293FT/SARS-CoV-2
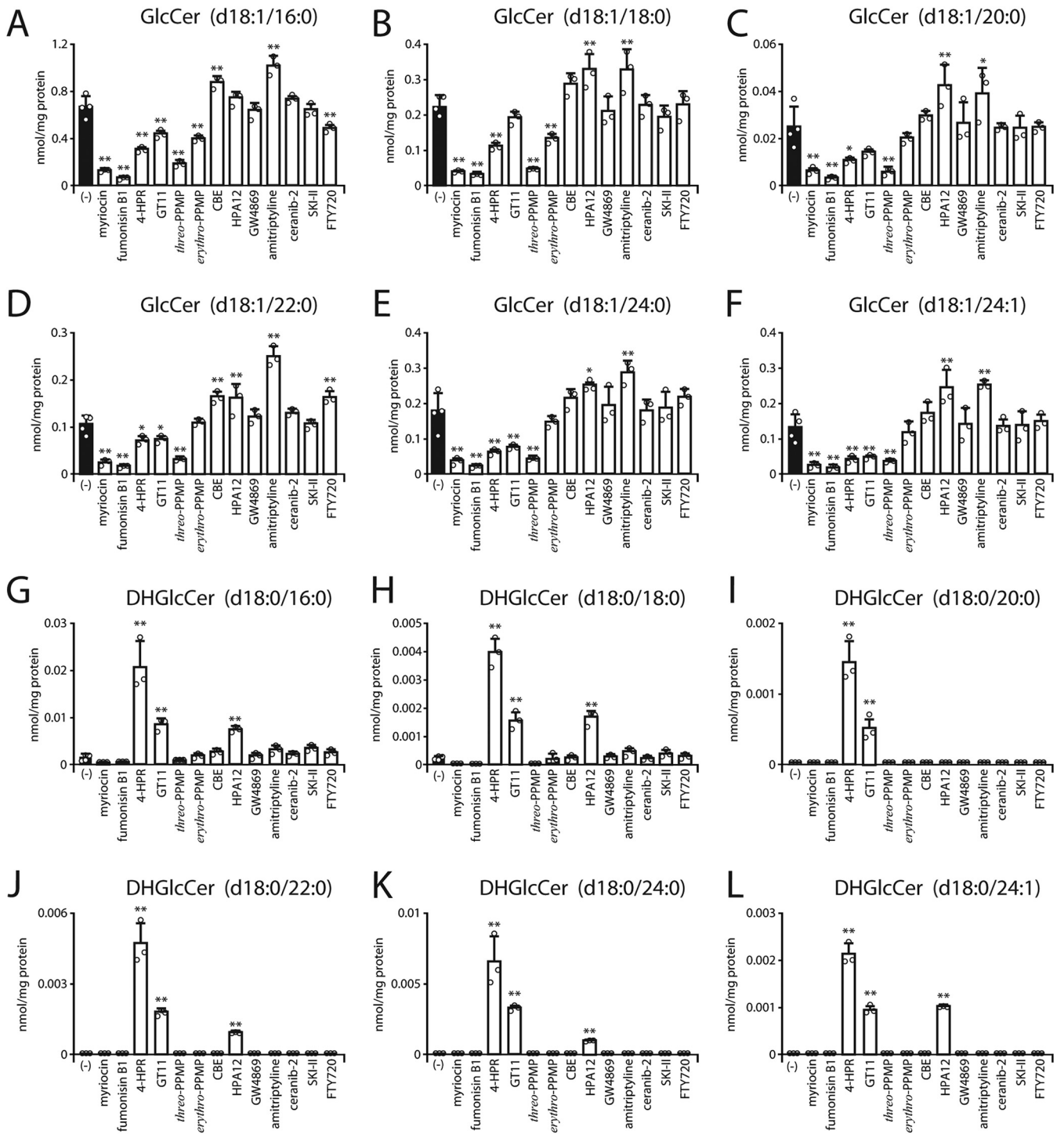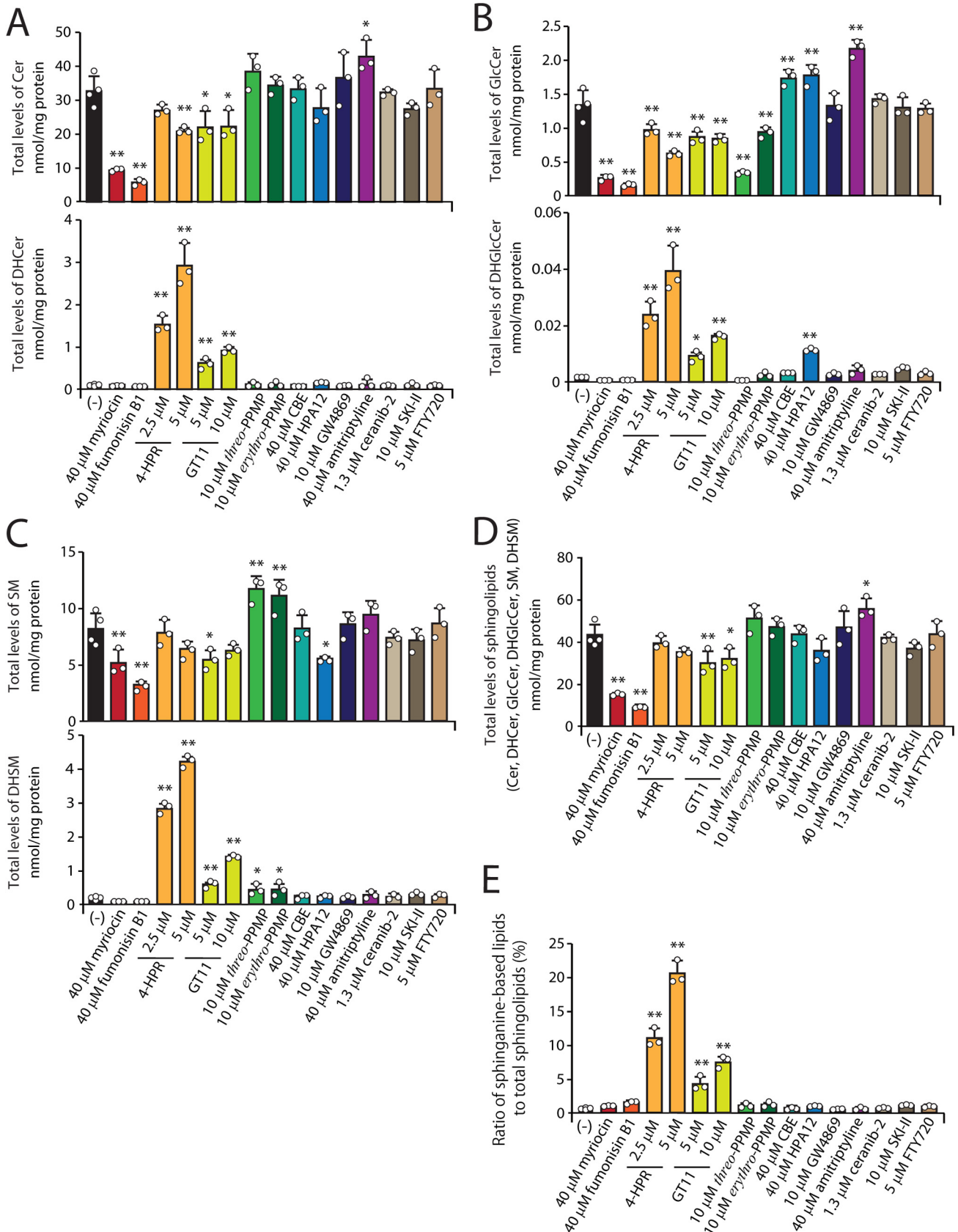
FIG 4 Effect of sphingolipid-metabolizing enzyme inhibitors on cellular GlcCer and DHGlcCer species in 293FT/ACE2/TMPRSS2/DSP1-7 cells. 293FT/ACE2/TMPRSS2/DSP1-7 cells were treated for 2 days with each of the compounds as follows: 40 μM myriocin, 40 μM fumonisin B1, 5 μM 4-HPR, 10 μM GT11, 10 μM *threo*-PPMP, 10 μM *erythro*-PPMP, 40 μM CBE, 40 μM HPA12, 10 μM GW4869, 40 μM amitriptyline, 1.3 μM ceranib-2, 10 μM SKI-II, and 5 μM FTY720. The cellular levels of GlcCer and DHGlcCer species with a distinct acyl chain were quantified using LC-MS/MS. The bar graphs show levels of GlcCer (A to F) and DHGlcCer (G to L). Statistical significance was determined using one-way ANOVA followed by Dunnett test for multiple comparisons; *, $P < 0.05$; **, $P < 0.01$ versus vehicle/DMSO-treated cells. Individual data points are shown as a scatterplot.

S/DSP8-11 cells (HEK293FT cells stably expressing SARS-CoV-2 S protein and DSP8-11), as effector cells, and 293FT/ACE2/TMPRSS2/DSP1-7 cells (HEK293FT cells stably expressing SARS-CoV-2 receptor angiotensin-converting enzyme 2 [ACE2], transmembrane serine protease 2 [TMPRSS2], and DSP1-7), as target cells, can be monitored by

FIG 5 Effect of sphingolipid-metabolizing enzyme inhibitors on cellular SM and DHSM species in 293FT/ACE2/TMPRSS2/DSP1-7 cells. 293FT/ACE2/TMPRSS2/DSP1-7 cells were treated for 2 days with each of the compounds as follows: 40 μM myriocin, 40 μM fumonisin B1, 5 μM 4-HPR, 10 μM GT11, 10 μM *threo*-PPMP (1-phenyl-2-palmitoylamino-3-morpholino-1-propanol), 10 μM *erythro*-PPMP, 40 μM CBE, 40 μM HPA12, 10 μM GW4869, 40 μM amitriptyline, 1.3 μM ceranib-2, 10 μM SKI-II, and 5 μM FTY720. The cellular levels of SM and DHSM species with a distinct acyl chain were quantified using LC-MS/MS. The bar graphs show levels of SM (A to F) and DHSM (G to L). Statistical significance was determined using one-way ANOVA followed by Dunnett test for multiple comparisons; *, *P* < 0.05, **, *P* < 0.01 versus vehicle/DMSO-treated cells. Individual data points are shown as a scatterplot.

measuring the activity of *Renilla* luciferase (RL), because of the DSP1-7 and DSP8-11 reassociation (25) (Fig. 2A). We assessed 13 compounds, including 12 inhibitors of enzymes involved in sphingolipid metabolism and an inactive stereoisomer of *threo*-PPMP (1-phenyl-2-palmitoylamino-3-morpholino-1-propanol; an inhibitor of GCS),

FIG 6 Effect of sphingolipid-metabolizing enzyme inhibitors on cellular sphingolipid levels. 293FT/ACE2/TMPRSS2/DSP1-7 cells were treated for 2 days with the indicated concentrations of the compounds. The cellular sphingolipid levels of compound-treated cells were quantified using liquid

(Continued on next page)

against SARS-CoV-2 S protein-mediated membrane fusion. Before evaluating the activity of compounds against cell-cell fusion, the nontoxic concentration of each compound for the cells was determined using a WST-8 [2-(2-methoxy-4-nitrophenyl)-3-(4-nitrophenyl)-5-(2, 4-disulfophenyl)-2H-tetrazolium, monosodium salt] assay, by enumerating the viable cells using a sensitive colorimetric method. When 293FT/ACE2/TMPRSS2/DSP1-7 cells were exposed to various concentrations of compounds for 2 days, cell viability remained unaffected for myriocin, fumonisin B1, conduritol B epoxide (CBE), HPA12, and amitriptyline at concentrations above 40 μM (Fig. 2B and Table 1). GT11, *threo*-PPMP, *erythro*-PPMP, GW4869, and SKI-II exhibited cytotoxicity above 20 μM; *N*-(4-hydroxyphenyl) retinamide (4-HPR) and FTY720 exhibited cytotoxicity above 10 μM; and ceranib-2 showed cytotoxicity above 2.5 μM.

We assessed the effects of the 13 compounds against the SARS-CoV-2 S protein-mediated cell-cell fusion at nontoxic concentrations of each compound (Fig. 2C and Table 1). The analysis of cell-cell fusion revealed that 4-HPR, *threo*-PPMP, and *erythro*-PPMP inhibited DSP activity by more than 50%, compared to that in the solvent-only control containing dimethyl sulfoxide (DMSO). Luciferase activity in cells harboring the preformed DSP1-7/DSP8-11 reporter complex was not affected by 4-HPR, *threo*-PPMP, and *erythro*-PPMP (Fig. 2D), indicating that the suppression of luciferase activity reflects the inhibition of cell-cell fusion by these compounds. However, little or no antimembrane fusion activity was found in the myriocin, fumonisin B1, GT11, CBE, HPA12, GW4869, amitriptyline, ceranib-2, SKI-II, and FTY720 treatments.

The levels of sphingolipid in inhibitor-treated cells were investigated by quantifying the sphingolipids using LC-MS/MS. Treatment with myriocin and fumonisin B1—inhibitors of *de novo* sphingolipid biosynthesis—significantly decreased the levels of most species with a distinct acyl chain in Cer, GlcCer, and SM (panels A to F in Fig. 3 to 5) and total levels of Cer, GlcCer, and SM (Fig. 6A to C, upper panels) compared with that in the DMSO treatment. Cells treated with myriocin and fumonisin B1 showed a reduction of approximately 65% and 79% in total sphingolipid levels, respectively (Fig. 6D). However, these changes had little effect on SARS-CoV-2 S protein-mediated cell-cell fusion, indicating that the total quantity of sphingolipid was not involved.

Contrary to our expectations, cells treated with 10 μM *erythro*-PPMP, an inactive stereoisomer of the GCS inhibitor *threo*-PPMP, exhibited decreased levels of GlcCer compared to the DMSO-treated cells, although to a lesser extent than the cells treated with *threo*-PPMP (Fig. 6B, upper panel). Myriocin and fumonisin B1 reduced the levels of all GlcCer species at levels comparable to or more than that by *threo*-PPMP (Fig. 4A to F); however, no correlation was observed between the GlcCer levels and the inhibition efficiency against cell-cell fusion. The inhibition of cell-cell fusion caused by 10 μM *threo*-PPMP and 10 μM *erythro*-PPMP could be potential off-target effects.

The levels of all species with a distinct acyl chain in DHCer, DHGlcCer, and DHSM (panels G to L in Fig. 3 to 5) and the total levels of DHCer, DHGlcCer, and DHSM (Fig. 6A to C, lower panels) increased in the 5 μM 4-HPR-treated cells, compared to that in the 10 μM GT11-treated cells, despite the fact that the two compounds inhibit the same enzyme, DES1. The ratio of saturated sphinganine-based lipids to total sphingolipids was close to 20% in 5 μM 4-HPR-treated cells and 10% in cells treated with 2.5 μM 4-HPR or 10 μM GT11 (Fig. 6E). The increased ratio was consistent with the inhibition efficiencies of cell-cell fusion (Fig. 2C and Fig. 6E).

4-HPR inhibits SARS-CoV-2 infection *in vitro*. We examined the antiviral activity of three compounds, 4-HPR, *threo*-PPMP, and *erythro*-PPMP, which inhibited SARS-CoV-2 S protein-mediated cell-cell fusion by more than 50%. In addition to these compounds,

FIG 6 Legend (Continued)
chromatography with LC-MS/MS analysis. (A) Cer (upper panel) and DHCer (lower panel). (B) GlcCer (upper panel) and DHGlcCer (lower panel). (C) SM (upper panel) and DHSM (lower panel). (D) Total sphingolipids (Cer, DHCer, GlcCer, DHGlcCer, SM, and DHSM). (E) Ratio of saturated sphinganine-based lipids (DHCer, DHGlcCer, and DHSM) to total sphingolipids. Values represent the mean $\pm$ SD from at least three independent experiments. Statistical significance was determined using one-way ANOVA followed by Dunnett test for multiple comparisons; *, $P < 0.05$; **, $P < 0.01$ versus vehicle/DMSO-treated cells. Individual data points are shown as a scatterplot.
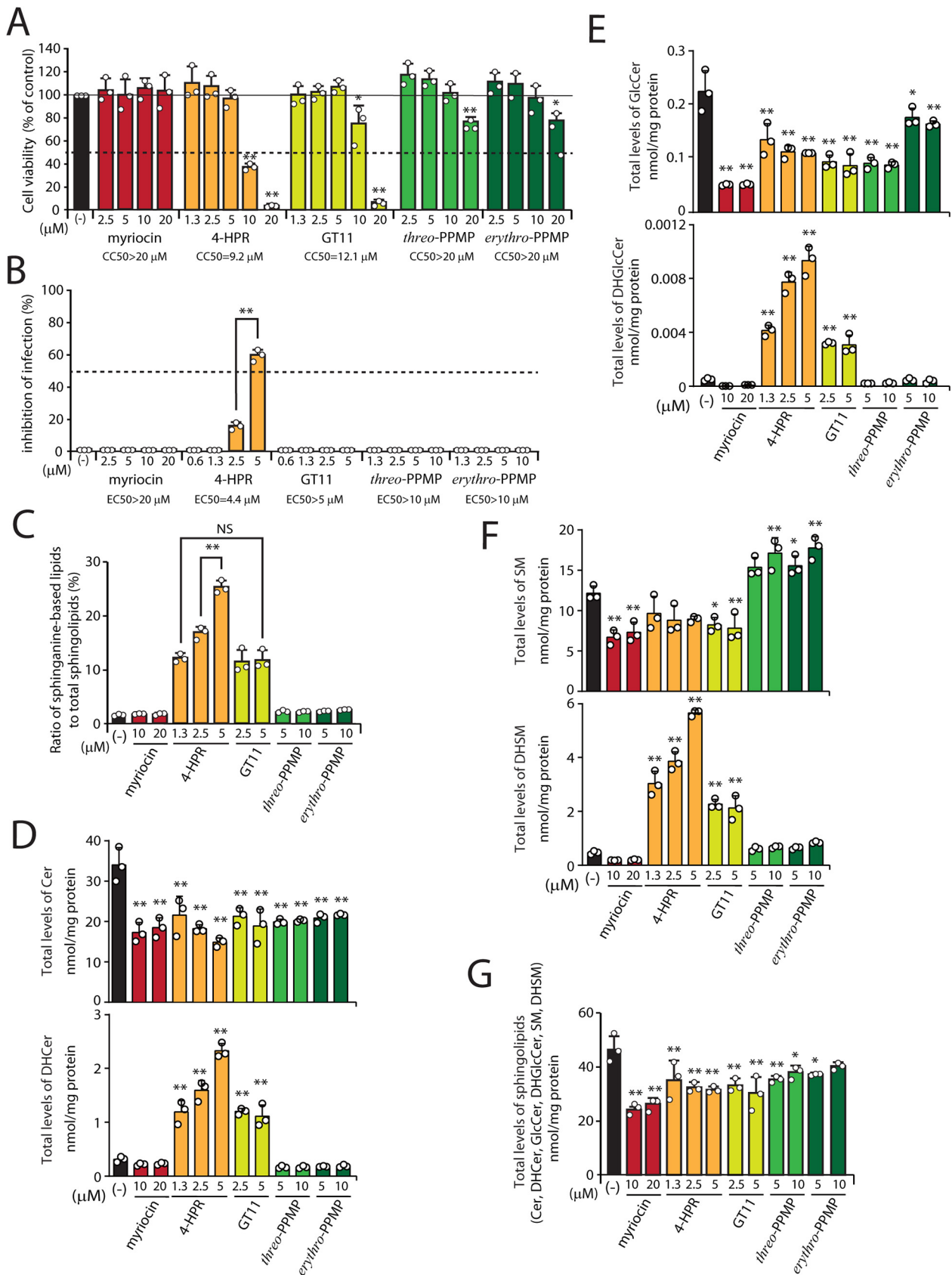
FIG 7 Effect of sphingolipid-metabolizing enzyme inhibitors on SARS-CoV-2 infection. VeroE6[TMPRSS2] cells were treated for 3 days with the indicated concentrations of compounds. (A) Cell viability was examined using the WST-8 assay. Results are normalized to the cell viability in

(Continued on next page)

myriocin and GT11 were also used to investigate the function of sphingolipids in viral infection. When VeroE6[TMPRSS2] cells were exposed to various concentrations of the compounds for 3 days, myriocin, at a concentration above $20\,\mu M$, exhibited no effect on cell viability (Fig. 7A). In contrast, *threo*-PPMP and *erythro*-PPMP exhibited cytotoxicity at concentrations above $20\,\mu M$, while 4-HPR and GT11 showed cytotoxicity above $10\,\mu M$.

We assessed the effects of the compounds against SARS-CoV-2 infection at nontoxic concentrations (Fig. 7B). 4-HPR exhibited potent antiviral activity against SARS-CoV-2 NCGM-05-2N strain (SARS-CoV-2[05-2N]) with a 50% effective concentration (EC_{50}) value of $4.4\,\mu M$, but GT11 did not. Cells treated with $5\,\mu M$ and $2.5\,\mu M$ 4-HPR inhibited viral infection by about 60% and 15%, respectively. However, no antiviral activity was observed at concentrations lower than $1.3\,\mu M$ 4-HPR or $5\,\mu M$ GT11.

The analysis of sphingolipid levels with LC-MS/MS revealed that the ratio of saturated sphinganine-based lipids to total sphingolipids in 4-HPR-treated cells increased in a concentration-dependent manner, exhibiting 25% for $5\,\mu M$ 4-HPR, 17% for $2.5\,\mu M$ 4-HPR, and 12% for $1.3\,\mu M$ 4-HPR treatment (Fig. 7C). No significant difference in the ratio of saturated sphinganine-based lipids to total sphingolipids was observed between $1.3\,\mu M$ 4-HPR and $5\,\mu M$ GT11 treatments (Fig. 7C). These results were consistent with the inhibition efficiencies of viral infection (Fig. 7B).

Myriocin, *threo*-PPMP, and *erythro*-PPMP did not exhibit antiviral activity (Fig. 7B). The cells treated with myriocin exhibited reduction in the total levels of Cer (Fig. 7D), GlcCer (Fig. 7E), and SM (Fig. 7F) and approximately 50% reduction in the total sphingolipid levels (Fig. 7G). The cells treated with *threo*-PPMP showed approximately 60% reduction in total GlcCer levels (Fig. 7E), compared to the cells treated with DMSO, indicating that myriocin and *threo*-PPMP inhibited their respective target enzymes. These results indicate that the total quantities of sphingolipids and GlcCer are not involved in SARS-CoV-2 infection.

4-HPR suppresses SARS-CoV-2 S-mediated membrane fusion by a DES1-independent mechanism. To elucidate the role of DES1 in SARS-CoV-2 S-mediated membrane fusion, we examined the effects of complementation with Cer, a reaction product of DES1, in 4-HPR treatment. The exogenously added cell-permeative C_8-Cer, the short-chain Cer analog containing short fatty acids (C_8), increased the cellular levels of C_8-Cer, C_8-GlcCer, and C_8-SM (data not shown), in a concentration-dependent manner. C_8-Cer treatment increased the levels of the native-chain-length C_{16^-}, C_{18^-}, and C_{20^-}Cers (Fig. 8A to F), which are reacylated via the salvage pathway (26). In addition, C_8-Cer treatment decreased the levels of the native DHCer (Fig. 8G to L), because C_8-Cer suppresses the *de novo* biosynthesis of sphingolipids, through SPT inhibition (27). The ratio of saturated sphinganine-based lipids to total sphingolipids in the 4-HPR- and $10\,\mu M$ C_8-Cer-treated cells decreased by approximately 74%, compared to that in the 4-HPR treated cells; this indicated that the changes in the sphingolipid profile induced by 4-HPR were mitigated by the supplementation with exogenous C_8-Cer (Fig. 8M). However, there was no significant differences in the cell-cell fusion efficiencies in the cells treated with 4-HPR and C_8-Cer, compared to that in the cells treated with 4-HPR (Fig. 8N).

We established DES1-knockout (KO) cells expressing ACE2, TMPRSS2, and DSP1-7, from HEK293T parental cells. FLAG tag-conjugated DES1-WT (FLAG-DES1-WT) or catalytically nonactive DES1 (FLAG-DES1-H89A/H93A) was overexpressed in DES1-KO cells for the DES1 KO-rescue experiment. Immunoblotting revealed that ACE2, TMPRSS2, and DSP1-7 were expressed at almost comparable levels in those cells, and DES1

FIG 7 Legend (Continued)

vehicle/DMSO-treated cells. (B) Antiviral activity was measured by reducing the SARS-CoV-2-induced cytopathic effect in VeroE6[TMPRSS2] cells. Results are expressed as the percentage of inhibition in compound-treated cells compared to that in the vehicle/DMSO-treated cells. (C) Ratio of saturated sphinganine-based lipids (DHCer, DHGlcCer, and DHSM) to total sphingolipids. (D) Cer (upper panel) and DHCer (lower panel). (E) GlcCer (upper panel) and DHGlcCer (lower panel). (F) SM (upper panel) and DHSM (lower panel). (G) Cellular levels of total sphingolipids (Cer, DHCer, GlcCer, DHGlcCer, SM, and DHSM). Values represent the mean $\pm$ SD from three independent experiments. Statistical significance was determined using one-way ANOVA followed by Dunnett test versus vehicle/DMSO-treated cells (A, D, E, F, and G) and Tukey-Kramer test (B and C); *, $P < 0.05$; **, $P < 0.01$. Individual data points are shown as a scatterplot.
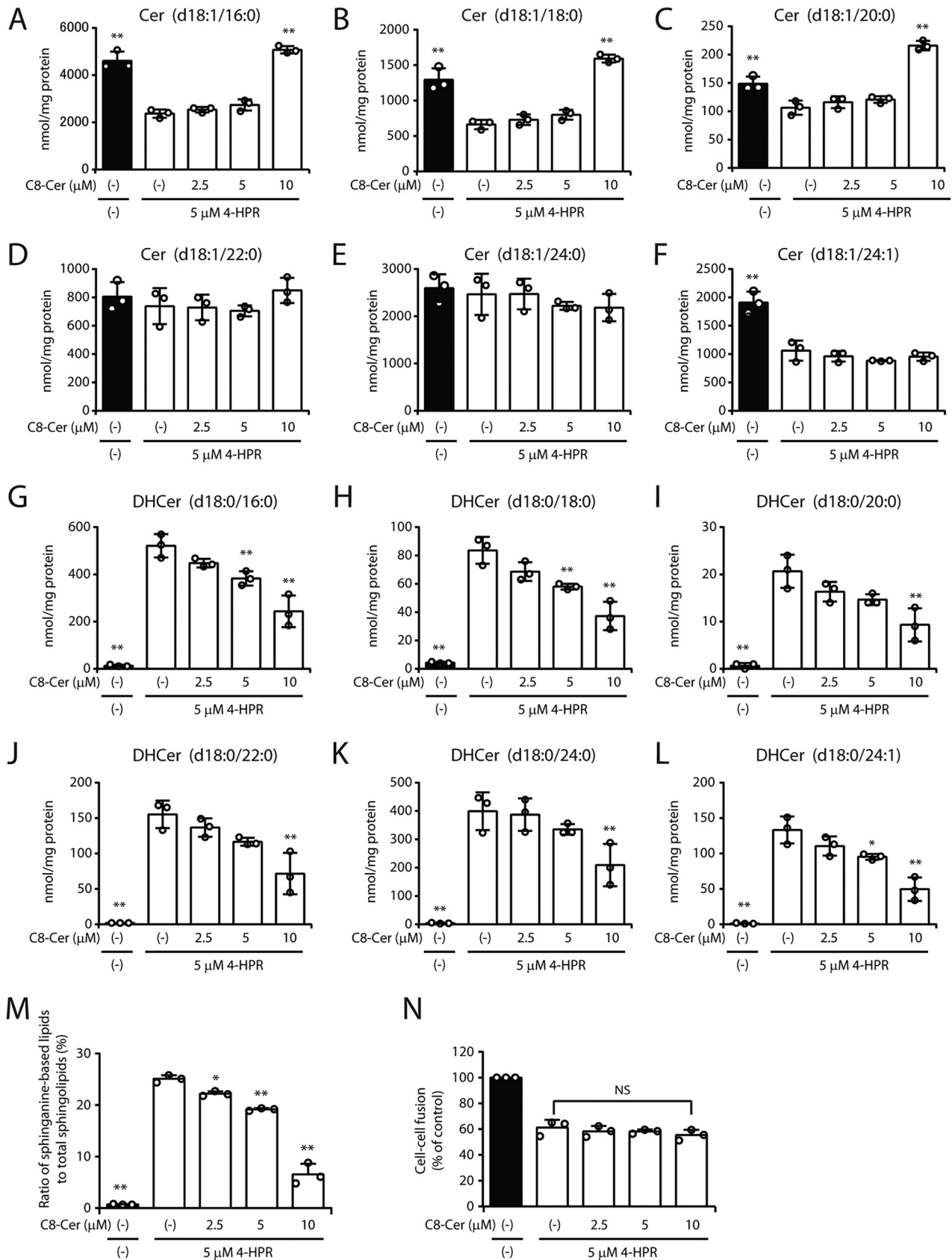
FIG 8 Effect of C_8-Cer complementation on 4-HPR treatment. 293FT/ACE2/TMPRSS2/DSP1-7 cells were treated for 2 days with the indicated concentrations of C_8-Cer and 5 μM 4-HPR. C_8-Cer was dissolved in ethanol and diluted to a final concentration of 0.2% ethanol in cell culture

expression was rescued in FLAG-DES1-WT- and FLAG-DES1-H89A/H93A-expressing cells (Fig. 9A). The LC-MS/MS analysis of sphingolipid levels showed that the ratio of saturated sphinganine-based lipids to total sphingolipids was 0.8% in WT HEK293T cells, 49% in DES1-KO cells, 12% in FLAG-DES1-WT-overexpressing DES1-KO cells, and 53% in FLAG-DES1-H89A/H93A-overexpressing DES1-KO cells (Fig. 9B). These results indicated the changes in the sphingolipid profile in DES1-KO cells; this was mitigated by the overexpression of FLAG-DES1-WT but not by that of FLAG-DES1-H89A/H93A. There were no significant differences among the cells in SARS-CoV-2 S-mediated cell-cell fusion (Fig. 9C). These results clearly indicated that DES1 is not involved in the inhibition of SARS-CoV-2 S-mediated membrane fusion.

4-HPR-treated cells display decreases in membrane fluidity. Finally, we examined the cellular effect of 4-HPR to obtain mechanistic insights into the inhibitory effect of 4-HPR on SARS-CoV-2 S protein-mediated cell-cell fusion and viral infection. Cell-cell fusion and viral infection were strictly dependent on the cell surface levels of the SARS-CoV-2 receptor ACE2, and therefore, we examined the effect of 4-HPR on the expression of ACE2 in 293FT/ACE2/TMPRSS2/DSP1-7 cells and VeroE6^{TMPRSS2} cells. No significant differences were observed in ACE2 expression levels in 293FT/ACE2/TMPRSS2/DSP1-7 cells treated with 5 μM 4-HPR compared with cells treated with DMSO or 10 μM GT11 (Fig. 10A). Similar results were obtained with VeroE6^{TMPRSS2} cells (Fig. 11A). These results indicate that the inhibition of cell-cell fusion and viral infection by 4-HPR is not attributable to ACE2 expression levels on the cell surface.

Lipid rafts are the detergent-resistant sphingolipid-rich microdomains of cellular membranes (28). Several viral receptors are localized in the lipid rafts and are involved in efficient viral infection (29, 30). We examined whether 4-HPR treatment affected the localization of ACE2 in the membrane microdomain. When we treated 293FT/ACE2/TMPRSS2/DSP1-7 cells with the nonionic detergent Triton X-100, ACE2 was found in the detergent-solubilized membrane fraction in which the nonraft marker transferrin receptor protein was localized, but not flotillin, the raft marker protein (Fig. 10B). Furthermore, ACE2 was not redistributed to the lipid raft domains even in the presence of SARS-CoV-2 S protein stimulation (Fig. 10B). Similar results were obtained with VeroE6^{TMPRSS2} cells (Fig. 11B). We observed no dramatic difference in ACE2 localization in the membrane microdomain between the DMSO and 4-HPR treatments (Fig. 10B), indicating that the inhibition of cell fusion by 4-HPR was not attributable to ACE2 localization on the membrane microdomain.

Membrane fluidity is associated with HIV-1 entry (31). We therefore examined the effect of 4-HPR on cellular membrane fluidity using lipophilic pyrene probes, which undergo excimer formation with increasing membrane fluidity (32). Cells treated with 5 μM and 2.5 μM 4-HPR exhibited decreased membrane fluidity by about 50% and 20%, respectively, compared with that of the DMSO-treated cells (Fig. 10C). In addition, membrane fluidity was not significantly different between cells treated with 2.5 μM 4-HPR and 10 μM GT11 (Fig. 10C), as well as the wild-type (WT) HEK293T and DES1-KO (Fig. 10D) cells. These results were consistent with the inhibition efficiencies of SARS-CoV-2 S protein-mediated cell-cell fusion (Fig. 2C and Fig. 9C). Similar results were obtained with VeroE6^{TMPRSS2} cells (Fig. 11C). These findings suggest that a decrease in cellular membrane fluidity by 4-HPR might be a major cause of the inhibition of SARS-CoV-2 infection.

DISCUSSION

In this study, we assessed several inhibitors of the enzymes functioning in sphingo-

FIG 8 Legend (Continued)

medium. The cellular levels of sphingolipid species with a distinct acyl chain were quantified by LC-MS/MS. (A to L) The bar graphs show levels of Cer (A to F) and DHCer (G to L). (M) Ratio of saturated sphinganine-based lipids (DHCer, DHGlcCer, and DHSM) to total sphingolipids. (N) The susceptibility of cell-cell fusion was examined using the DSP-based cell-cell fusion assay. Results are normalized to the rate of cell-cell fusion in vehicle/DMSO- and ethanol-treated cells. Values represent the mean ± SD from three independent experiments. Statistical significance was determined using one-way ANOVA followed by Dunnett test versus 5 μM 4-HPR-treated cells without C$_8$-Cer complementation; *, $P < 0.05$; **, $P < 0.01$; NS, not significant. Individual data points are shown as a scatterplot.
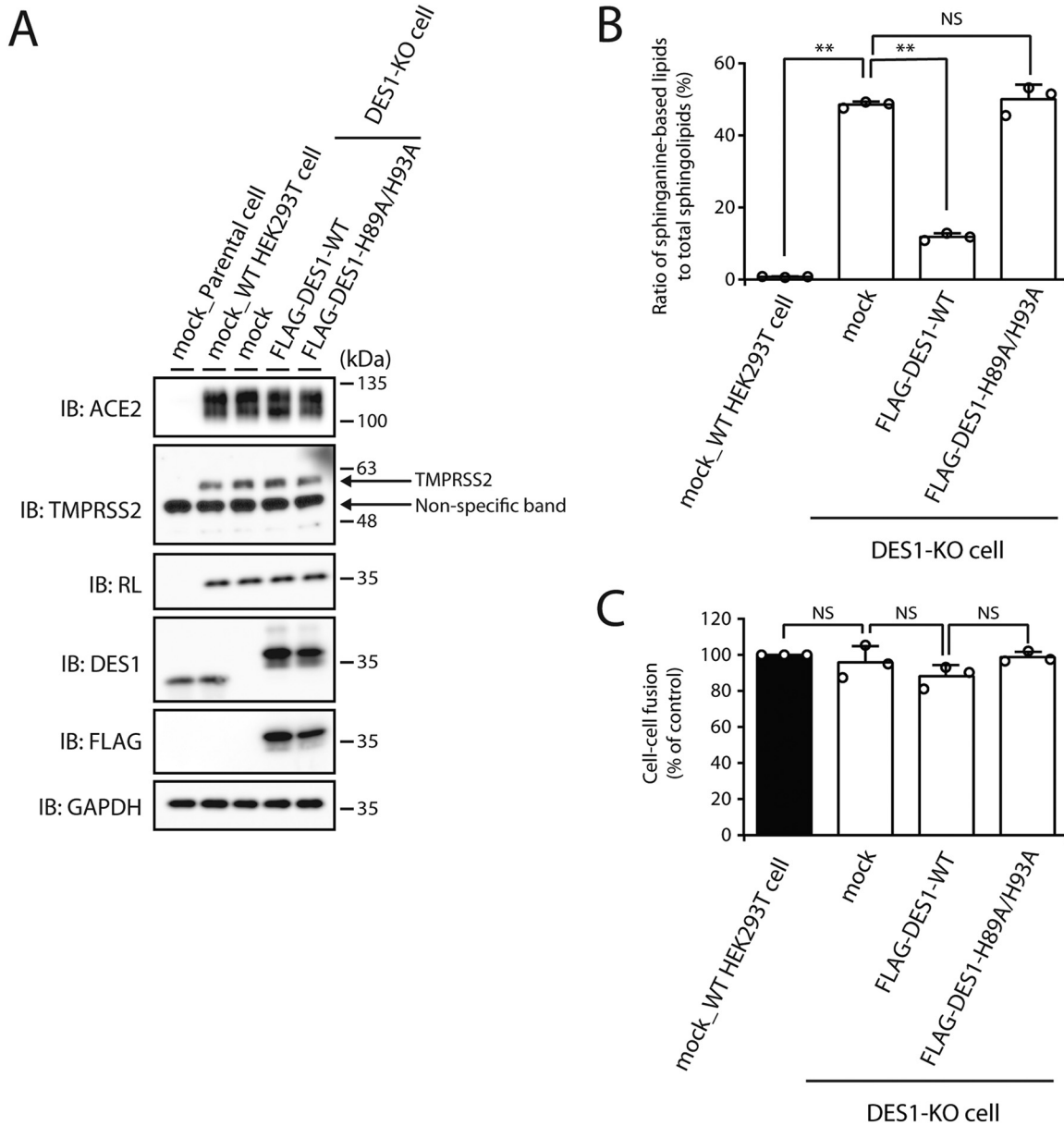
FIG 9 Effects of DES1-KO cells on cellular sphingolipid levels and SARS-CoV-2 S protein-mediated membrane fusion. WT HEK293T cells and DES1-KO cells stably expressing ACE2, TMPRSS2, and DSP1-7 were transfected with the following plasmids: empty vector (mock), 3×FLAG-tagged WT DES1 (FLAG-DES1-WT), or 3×FLAG-tagged catalytically inactive DES1 mutant (FLAG-DES1-H89A/H93A). The cells were cultured for an additional 48 h and used for the experiments as described below. (A) Cells were lysed and analyzed through immunoblotting (IB) with the indicated antibodies. Parental HEK293T cells were included as the control. One representative experiment is shown, and similar results were obtained in three independent experiments. (B) The cellular sphingolipid levels of compound-treated cells were quantified using liquid chromatography with LC-MS/MS analysis. Ratio of saturated sphinganine-based lipids (DHCer, DHGlcCer, and DHSM) to total sphingolipids. (C) The susceptibility of cell-cell fusion was examined using the DSP-based cell-fusion assay. Results are normalized to the rate of cell-cell fusion in WT HEK293T cells transfected with empty vector. Values represent the mean ± SD from three independent experiments. Statistical significance was determined using one-way ANOVA followed by Tukey-Kramer test (B and C); **, $P < 0.01$; NS, not significant. Individual data points are shown as a scatterplot.

lipid metabolism, against SARS-CoV-2 S-mediated cell-cell fusion and viral infection. No significant activity against cell-cell fusion or viral infection was found for myriocin, although the total sphingolipid levels significantly decreased in myriocin-treated cells compared with that in the DMSO-treated cells. Lipid rafts, sphingolipid-enriched microdomains in cellular membranes, were not a major localization site for ACE2 in 293FT/ACE2/TMPRSS2/DSP1-7 cells and VeroE6^TMPRSS2 cells. This may explain why the quantity
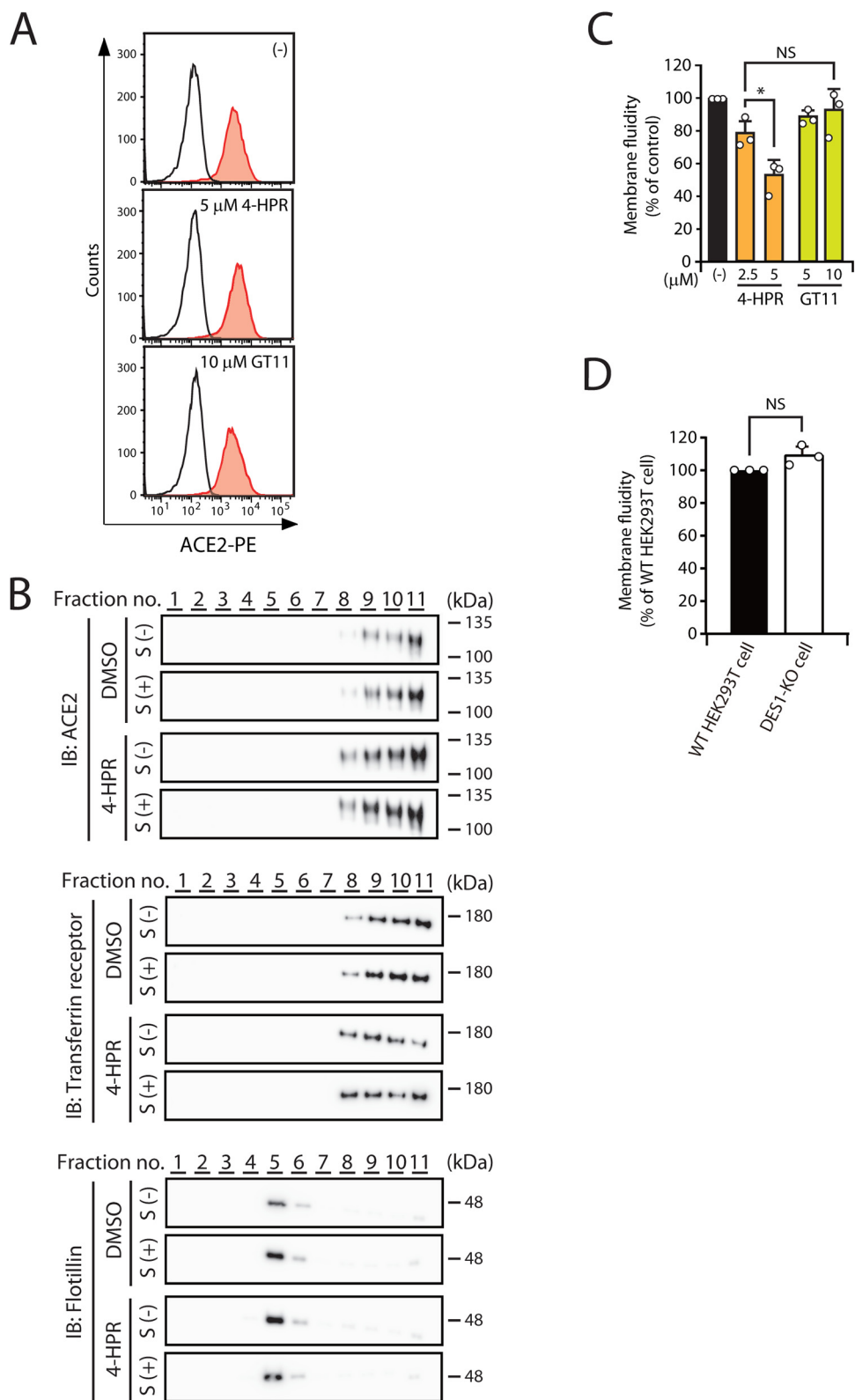
FIG 10 Effect of 4-HPR on cell-surface levels of ACE2, localization of ACE2 in membrane microdomains, and membrane fluidity. 293FT/ACE2/TMPRSS2/DSP1-7 cells were treated for 2 days with the indicated concentrations of compounds. (A) Cell surface expression levels of ACE2 in compound-treated cells were analyzed using flow cytometry with an anti-ACE2 antibody (filled histogram). Open histograms indicate the isotype control. One representative experiment is shown, and similar results were obtained in three independent experiments. (B) Isolation of lipid rafts. Target cells were stimulated for 30 min with or without SARS-CoV-2 spike (S) protein-expressing cells, denoted by S

(Continued on next page)

of sphingolipids did not appear to influence the SARS-CoV-2 infection. ACE2 is localized within the nonraft domains in Chinese hamster ovary cells (33) and VeroE6 cells (34), while there are some reports on the ACE2 localization within raft domains in VeroE6 cells (35, 36). The cause of the discrepancies between these findings is unknown. In this study, ACE2 did not redistribute to the lipid raft domains even in the presence of SARS-CoV-2 S protein stimulation. Therefore, we propose that ACE2 localization on the membrane microdomain is not essential for SARS-CoV-2 entry into host cells, at least in our infection study.

4-HPR suppressed SARS-CoV-2 S-mediated membrane fusion by a DES1-independent mechanism. The antiviral activity of 4-HPR is proved in different viruses, such as vesicular stomatitis virus (data not shown), HIV (37), dengue virus (DENV) (38), and Zika virus (39). 4-HPR inhibited DENV replication through blocking the association of the viral RNA-dependent RNA polymerase (nonstructural protein 5) and the host's nuclear transport factors, importin $\alpha/\beta 1$ (38); however, the mechanism underlying the inhibition of viral entry by 4-HPR remains unclear. 4-HPR decreased the cell membrane fluidity; however, the direct cause of the reduced membrane fluidity and the relationship between fluidity and reduced viral infection are currently unclear. It was known that 4-HPR increased the levels of reactive oxygen species (ROS) intracellularly (40), and lipid peroxides generated by ROS caused membrane fluidity (41). We hypothesize that the inhibitory effect of 4-HPR on viral infections may be related to ROS production. Further investigation is needed to elucidate the precise mechanism underlying the inhibition in SARS-CoV-2 S-mediated membrane fusion, by 4-HPR.

4-HPR potently inhibited SARS-CoV-2 S protein-mediated membrane fusion in a cell-cell fusion assay system ($EC_{50} = 4.1\,\mu M$) and the viral infection *in vitro* ($EC_{50} = 4.4\,\mu M$). 4-HPR is a synthetic derivative of all-*trans*-retinoic acid, which is widely investigated as a cancer treatment (42–45). In a phase I study, where 4-HPR was administered as an oral powder to patients with relapsed/refractory neuroblastoma, the day 6 mean peak plasma concentration was $21\,\mu M$ 4-HPR at a dose of $1,500\,mg/m^2$ per day (42). The EC_{50} value for 4-HPR against SARS-CoV-2 infection was below its plasma concentration ($4.4\,\mu M$ versus $21\,\mu M$) in this study, and therefore, 4-HPR could be a potential therapeutic agent for COVID-19, as predicted previously (46). 4-HPR exhibited a low-toxicity profile in many clinical trials and in long-term treatments (42–45). Therefore, the results from this study, together with the accumulated clinical data regarding the safety of 4-HPR, make it a potential candidate drug to treat COVID-19. In addition, 4-HPR could be used for prophylactic therapy against SARS-CoV-2 infection. It could be administered via an inhaler or a spray to the airways, perhaps by self-administration, unlike the vaccines. This could relieve the pressure on the health care system.

MATERIALS AND METHODS

Cells and viruses. HEK293FT cells expressing the SARS-CoV-2 S protein and DSP8-11 (293FT/SARS-CoV-2 S/DSP8-11) were maintained in Dulbecco's modified Eagle medium (DMEM) supplemented with 10% fetal calf serum (FCS), $100\,\mu g/ml$ penicillin, $100\,\mu g/ml$ streptomycin, $1\,\mu g/ml$ puromycin, and $10\,\mu g/ml$ blasticidin. HEK293FT cells expressing ACE2, TMPRSS2, and DSP1-7 (293FT/ACE2/TMPRSS2/DSP1-7) were maintained in DMEM supplemented with 10% FCS, $100\,\mu g/ml$ penicillin, $100\,\mu g/ml$ streptomycin, $1\,\mu g/ml$ puromycin, $10\,\mu g/ml$ blasticidin, and $300\,\mu g/ml$ hygromycin. HEK293FT cells expressing DSP8-11 (293FT/DSP8-11) were maintained in DMEM supplemented with 10% FCS, $100\,\mu g/ml$ penicillin, $100\,\mu g/ml$ streptomycin, and $1\,\mu g/ml$ puromycin. WT HEK293T cells and DES1-KO cells expressing ACE2, TMPRSS2, and DSP1-7 were established from a WT HEK293T cell line (ab255449) and a DES1-KO HEK293T cell line (ab266481), respectively; those cell lines were obtained from Abcam (Cambridge, United Kingdom).

FIG 10 Legend (Continued)

(+) and S (−), respectively. Sucrose gradients were harvested in 1-ml fractions (fraction 1, top of the gradient; fraction 11, bottom of the gradient), and each fraction was analyzed using SDS-PAGE and immunoblotted with anti-ACE2, anti-transferrin receptor (nonraft marker), or antiflotillin (raft marker) antibodies. One representative experiment is shown, and similar results were obtained in three independent experiments. (C and D) Membrane fluidity was examined using a fluorescent lipophilic pyrene probe. Results are normalized to the membrane fluidity in the vehicle/DMSO-treated cells. Values represent the mean ± SD from three independent experiments. Statistical significance was determined using one-way ANOVA followed by Dunnett test versus vehicle/DMSO-treated cells; NS, not significant. Individual data points are shown as a scatterplot.
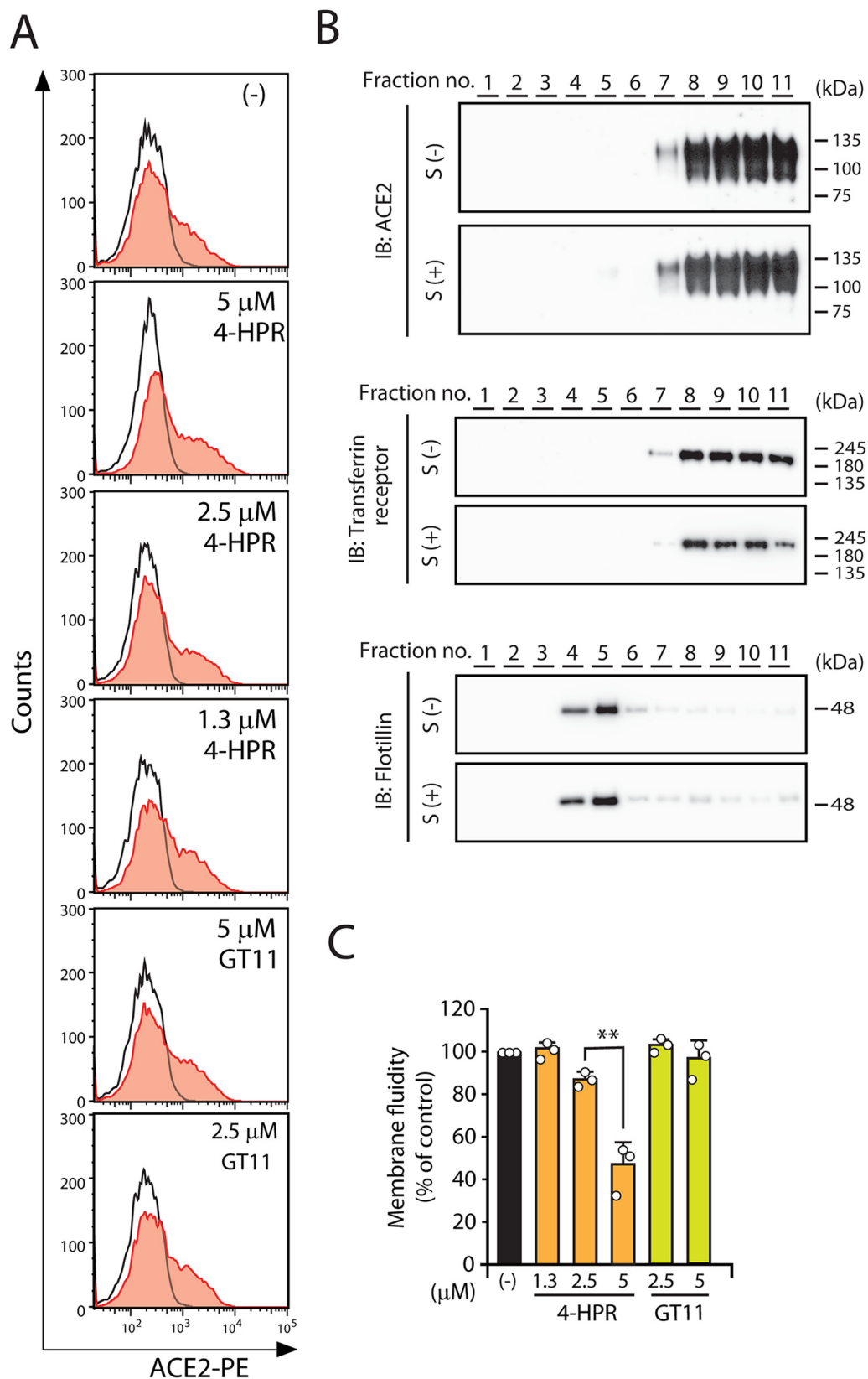
FIG 11 Effect of 4-HPR on cell-surface levels of ACE2 and membrane fluidity in VeroE6[TMPRSS2] cells. (A) VeroE6[TMPRSS2] cells were treated for 3 days with the indicated concentrations of the compounds. Cell surface expression levels of ACE2 in compound-treated cells were analyzed by flow cytometry using an anti-ACE2 antibody (filled histogram). Open histograms indicate the isotype control. One representative experiment is shown, and similar results were

(Continued on next page)

VeroE6^{TMPRSS2} cells were obtained from the Japanese Collection of Research Bioresources Cell Bank (Osaka, Japan) (47). VeroE6^{TMPRSS2} cells were maintained in DMEM supplemented with 10% FCS, 100 μg/ml of penicillin, 100 μg/ml of streptomycin, and 1 mg/ml of Geneticin antibiotic. SARS-CoV-2 NCGM-05-2N strain (SARS-CoV-2^{05-2N}) was isolated from nasopharyngeal swabs of a patient with COVID-19, who was admitted to the National Center for Global Health and Medicine, Tokyo, Japan.

Chemicals and antibodies. Myriocin, SKI-II, and FTY720 were obtained from Abcam. Fumonisin B1, CBE, amitriptyline, and ceranib-2 were obtained from Sigma-Aldrich (St. Louis, MO, USA). 4-HPR and HPA12 were obtained from Tokyo Chemical Industry (Tokyo, Japan). GT11 was obtained from Avanti Polar Lipids (Alabaster, AL, USA). DL-*threo*-PPMP, DL-*erythro*-PPMP, and GW4869 were obtained from Cayman Chemical (Ann Arbor, MI, USA). All compounds were dissolved in DMSO and diluted to a final concentration of 0.2% DMSO in cell culture medium.

Mouse IgG monoclonal anti-FLAG antibody (catalog no. 014-22383) and mouse IgG monoclonal anti-glyceraldehyde 3-phosphate dehydrogenase (anti-GAPDH) antibody (catalog no. 014-25524) were obtained from Fujifilm (Tokyo, Japan). Mouse IgG1 monoclonal anti-ACE2 antibody (catalog no. 66699-1-Ig) was obtained from Proteintech (Rosemont, IL, USA). Mouse IgG1 isotype control was obtained from BioLegend (San Diego, CA, USA). Goat phycoerythrin (PE)-conjugated anti-mouse IgG polyclonal antibody (catalog no. 12-4010-82) was obtained from Thermo Fisher Scientific (Waltham, MA, USA). *N*-Palmitoyl-d31-*d-erythro*-sphingosine (D31-Cer) and *N*-palmitoyl-d31-*d-erythro*-sphingosylphosphorylcholine (D31-SM) were obtained from Avanti Polar Lipids, and *N*-omega-d3-hexadecanoyl-glucopsychosine (D3-GlcCer) was obtained from Cayman Chemical.

N-Octanoyl-*d-erythro*-sphingosine (C$_8$-Cer), rabbit polyclonal anti-ACE2 antibody (catalog no. ab15348), rabbit IgG monoclonal anti-TMPRSS2 antibody (catalog no. ab92323), rabbit IgG monoclonal anti-RL antibody (catalog no. ab236020), rabbit IgG monoclonal anti-DES1 antibody (catalog no. ab167169), rabbit IgG monoclonal anti-transferrin receptor antibody (catalog no. ab214039), and rabbit IgG monoclonal anti-flotillin 1 antibody (catalog no. ab133497) were obtained from Abcam. Goat horseradish peroxidase-conjugated anti-rabbit IgG antibody (catalog no. 7074S) was obtained from Cell Signaling Technology (Beverly, MA, USA).

Cytotoxicity assay. 293FT/ACE2/TMPRSS2/DSP1-7 and VeroE6^{TMPRSS2} cells were seeded in 96-well plates at 1×10^4 cells/well and 5×10^3 cells/well, respectively. On the following day, the cells were cultured with the specific compounds for 2 days (293FT/ACE2/TMPRSS2/DSP1-7 cells) or 3 days (VeroE6^{TMPRSS2} cells), and the 50% cytotoxic concentration (CC$_{50}$) values were determined using the WST-8 assay employing Cell Counting kit 8 (Dojindo, Kumamoto, Japan).

DSP-based cell-cell fusion assay. The cell-cell fusion assay was conducted as previously described (25), with slight modifications. Target cells (293FT/ACE2/TMPRSS2/DSP1-7) and effector cells (293FT/SARS-CoV-2 S/DSP8-11) were seeded in 24-well plates at 4×10^4 cells/well. On the following day, the medium of the target cells was exchanged with DMEM containing 10% FCS and various concentrations of each of the compounds to be tested, and the cells were incubated for an additional 2 days. Cells were washed with phosphate-buffered saline (PBS) and were detached using Cellstripper containing EDTA but no trypsin (Corning, Christiansburg, VA, USA). Cells were resuspended in serum-free DMEM and centrifuged at $500 \times g$ for 2 min. After aspirating the supernatant, the cells were resuspended in serum-free DMEM containing 1% Nutridoma SP (Roche, Basel, Switzerland) and 6 μM EnduRen (Promega, Madison, WI, USA), a substrate for RL. The effector and target cells were mixed in the wells of a 96-well plate, and after incubating at 37°C for 4 h, the RL activity was measured using a SpectraMax i3x microplate reader (Molecular Devices, San Jose, CA, USA).

Antiviral assay. VeroE6^{TMPRSS2} cells were seeded in 96-well plates (5×10^3 cells/well). On the following day, the cells were cultured with each of the tested compounds for 3 days before adding SARS-CoV-2^{05-2N}. The cells were inoculated at a multiplicity of infection of 0.01. After culturing the cells with the specific compounds and SARS-CoV-2^{05-2N} for 3 days, the level of cytopathic effect observed in SARS-CoV-2-exposed cells was determined using the WST-8 assay.

Lipid extraction and quantification of sphingolipids by LC-MS/MS. Lipid extraction and quantification of sphingolipids by LC-MS/MS were performed as described previously (48–50). 293FT/ACE2/TMPRSS2/DSP1-7 and VeroE6^{TMPRSS2} cells were seeded in 6-well plates at 2×10^5 cells/well and 7×10^4 cells/well, respectively. On the following day, the cells were cultured with each of the tested compounds for 2 days (293FT/ACE2/TMPRSS2/DSP1-7 cells) or 3 days (VeroE6^{TMPRSS2} cells), after which the cells were washed once with cold PBS, collected in 100 μl of cold PBS, and then homogenized using sonication. Part of the sample (5 μl) was used in the bicinchoninic acid protein assay to determine the amount of protein. Total lipids were extracted by adding 375 μl of chloroform-methanol (1:2, vol/vol) containing

FIG 11 Legend (Continued)

obtained in three independent experiments. (B) Isolation of lipid rafts. VeroE6^{TMPRSS2} cells were stimulated for 30 min with or without SARS-CoV-2 spike (S) protein-expressing cells, denoted by S (+) and S (−), respectively. Sucrose gradients were harvested in 1-ml fractions (fraction 1, top of the gradient; fraction 11, bottom of the gradient), and each fraction was analyzed by SDS-PAGE and immunoblotted with anti-ACE2, anti-transferrin receptor (nonraft marker), or antiflotillin (raft marker) antibodies. One representative experiment is shown, and similar results were obtained in three independent experiments. (C) VeroE6^{TMPRSS2} cells were treated for 3 days with the indicated concentrations of the compounds. Membrane fluidity of compound-treated cells was examined with a fluorescent lipophilic pyrene probe. Results are normalized to the rate of membrane fluidity in vehicle/DMSO-treated cells. Values represent the mean $\pm$ SD from three independent experiments. Statistical significance was determined by one-way ANOVA followed by the Tukey-Kramer test; **, $P < 0.01$. Individual data points are shown as a scatterplot.

40 pmol of each component, specifically D31-Cer, D31-SM, and D3-GlcCer. Deuterated D31-Cer, D31-SM, and D3-GlcCer were used as internal standards for Cer and DHCer, SM and DHSM, and GlcCer and DHGlcCer, respectively. After sonicating the single-phase mixture, 100 μl of chloroform-methanol-5 N NaOH (1:2:0.8, vol/vol/vol) was added and the solution was incubated for 1 h at 37°C, followed by neutralization with acetic acid. Subsequently, 158 μl of chloroform and 158 μl of water were added and the mixture was vigorously vortexed, before centrifuging for 1 min at 13,000 $\times$ g at 4°C. The lower phase was withdrawn and dried and then resuspended in acetonitrile-methanol (1:1, vol/vol), sonicated for 10 s, and centrifuged at 14,000 $\times$ g for 5 min, and the supernatant was transferred to vials. The concentrations of Cer, DHCer, GlcCer, DHGlcCer, SM, and DHSM were analyzed using the QTRAP4500 instrument (Sciex, Framingham, MA, USA). Sphingolipids containing $C_{16:0}$, $C_{18:0}$, $C_{20:0}$, $C_{22:0}$, $C_{24:0}$, and $C_{24:1}$ fatty acids were detected using a multiple-reaction monitoring method.

Analysis of cell surface expression of ACE2. 293FT/ACE2/TMPRSS2/DSP1-7 cells in 24-well plates were treated with the indicated concentrations of the compounds for 2 days. Cells were harvested using Cellstripper (Corning) and fixed with 4% formaldehyde before incubation with either anti-ACE2 antibody (Proteintech) or mouse IgG1 isotype control (BioLegend) antibody at 4°C. Cells were stained with PE-conjugated secondary antibody (Thermo Fisher Scientific) and analyzed using the FACSCanto II instrument (BD Biosciences, San Jose, CA, USA). Data were analyzed using the FlowJo software (Tree Star Inc., San Carlos, CA, USA).

S protein stimulation of 293FT/SARS-CoV-2 S/DSP8-11 cells and isolation of lipid raft domains. Target cells (293FT/ACE2/TMPRSS2/DSP1-7), S protein-expressing cells (293FT/SARS-CoV-2 S/DSP8-11), and cells not expressing S protein (293FT/DSP8-11) were seeded at 7×10^5 cells per 10-cm-diameter dish. On the following day, the medium of the target cells was exchanged with DMEM containing 10% FCS and 5 μM 4-HPR, and the cells were incubated for an additional 2 days. Cells were then washed with PBS and detached using Cellstripper (Corning) before resuspending in serum-free DMEM and centrifuging at 500 $\times$ g for 2 min. After aspirating the supernatant, the cells were resuspended in serum-free DMEM containing 1% Nutridoma SP (Roche). The target cells were mixed with 293FT/SARS-CoV-2 S/DSP8-11 (presence of SARS-CoV-2 S protein stimulation) or 293FT/DSP8-11 (absence of SARS-CoV-2 S protein stimulation) cells, incubated for 30 min, and then washed with cold PBS. Subsequently, sucrose gradient analysis for ACE2 was performed as described previously (51), with slight modifications. The pellets were homogenized in 2 ml of TNE buffer (25 mM Tris-HCl, pH 7.5, 150 mM NaCl, and 1 mM EDTA) with 0.1% Triton X-100. The sucrose content of the homogenate was then adjusted to 40% by adding 80% sucrose. A linear sucrose gradient (5 to 30%) in 7 ml of TNE buffer without Triton X-100 was layered over the lysate. The gradients were centrifuged for 17 h at 200,000 $\times$ g at 4°C using a P40ST rotor (Hitachi Koki Co., Ltd., Tokyo, Japan). Eleven fractions were collected from the top of the gradient, followed by immunoblot analysis using anti-ACE2, anti-transferrin receptor (nonraft marker), and anti-flotillin 1 (raft marker) antibodies (all from Abcam).

Analysis of cellular membrane fluidity. Analysis of membrane fluidity was performed as described previously (52), with slight modifications. Briefly, 293FT/ACE2/TMPRSS2/DSP1-7 cells in 24-well plates were treated with the indicated concentrations of the compounds for 2 days. Cells were detached using Cellstripper (Corning), resuspended in PBS, and centrifuged at 500 $\times$ g for 2 min. The supernatant was aspirated, and the cells were labeled using a solution of 15 μM pyrenedecanoic acid and 0.08% F-127 in perfusion buffer, in the dark for 20 min with rocking at 25°C. Excess probe was removed, and the cells were washed with PBS. The cells were resuspended in 450 μl PBS; 200 μl was aliquoted into a 96-well plate, and fluorescence was measured using an excitation wavelength of 350 nm and two emission wavelengths: 400 nm for the monomer and 470 nm for the excimer, using a SpectraMax i3x microplate reader (Molecular Devices). The ratio of excimer to monomer fluorescence is related to cellular membrane fluidity, with a higher ratio reflecting greater fluidity.

Statistical analysis. All statistical analyses were performed with GraphPad Prism 6 (GraphPad Software, San Diego, CA, USA). For comparisons, we conducted one-way analysis of variance (ANOVA) followed by Dunnett test or Tukey-Kramer test. The results are shown as the mean $\pm$ SD. P values of <0.05 were considered statistically significant.

REFERENCES

1. Zhu N, Zhang D, Wang W, Li X, Yang B, Song J, Zhao X, Huang B, Shi W, Lu R, Niu P, Zhan F, Ma X, Wang D, Xu W, Wu G, Gao GF, Tan W. 2020. A novel coronavirus from patients with pneumonia in China, 2019. New Engl J Med 382:727–733. https://doi.org/10.1056/NEJMoa2001017.

2. Zhou P, Yang XL, Wang XG, Hu B, Zhang L, Zhang W, Si HR, Zhu Y, Li B, Huang CL, Chen HD, Chen J, Luo Y, Guo H, Jiang RD, Liu MQ, Chen Y, Shen XR, Wang X, Zheng XS, Zhao K, Chen QJ, Deng F, Liu LL, Yan B, Zhan FX, Wang YY, Xiao GF, Sh ZL. 2020. A pneumonia outbreak associated with a new coronavirus of probable bat origin. Nature 579:270–273. https://doi.org/10.1038/s41586-020-2012-7.

3. Li Q, Guan X, Wu P, Wang X, Zhou L, Tong Y, Ren R, Leung KSM, Lau EHY, Wong JY, Xing X, Xiang N, Wu Y, Li C, Chen Q, Li D, Liu T, Zhao J, Liu M, Tu W, Chen C, Jin L, Yang R, Wang Q, Zhou S, Wang R, Liu H, Luo Y, Liu Y, Shao G, Li H, Tao Z, Yang Y, Deng Z, Liu B, Ma Z, Zhang Y, Shi

G, Lam TTY, Wu JT, Gao GF, Cowling BJ, Yang B, Leung GM, Feng Z. 2020. Early transmission dynamics in Wuhan, China, of novel coronavirus-infected pneumonia. N Engl J Med 382:1199–1207. https://doi.org/10.1056/NEJMoa2001316.

4. Mitsuya H, Kokudo N. 2020. Sustaining containment of COVID-19: global sharing for pandemic response. Glob Health Med 2:53–55. https://doi.org/10.35772/ghm.2020.01040.

5. Grassmé H, Riehle A, Wilker B, Gulbins E. 2005. Rhinoviruses infect human epithelial cells via ceramide-enriched membrane platforms. J Biol Chem 280:26256–26262. https://doi.org/10.1074/jbc.M500835200.

6. Drews K, Calgi MP, Harrison WC, Drews CM, Costa-Pinheiro P, Shaw JJP, Jobe KA, Han JD, Fox TE, White JM, Kester M. 2020. Glucosylceramide synthase maintains influenza virus entry and infection. PLoS One 15:e0228735. https://doi.org/10.1371/journal.pone.0228735.

7. Weng L, Hirata Y, Arai M, Kohara M, Wakita T, Watashi K, Shimotohno K, He Y, Zhong J, Toyoda T. 2010. Sphingomyelin activates hepatitis C virus RNA polymerase in a genotype-specific manner. J Virol 84:11761–11770. https://doi.org/10.1128/JVI.00638-10.

8. Kanj SS, Dandashi N, El-Hed A, Harik H, Maalouf M, Kozhaya L, Mousallem T, Tollefson AE, Wold WS, Chalfant CE, Dbaibo GS. 2006. Ceramide regulates SR protein phosphorylation during adenoviral infection. Virology 345:280–289. https://doi.org/10.1016/j.virol.2005.09.060.

9. Hayashi Y, Nemoto-Sasaki Y, Tanikawa T, Oka S, Tsuchiya K, Zama K, Mitsutake S, Sugiura T, Yamashita A. 2014. Sphingomyelin synthase 2, but not sphingomyelin synthase 1, is involved in HIV-1 envelope-mediated membrane fusion. J Biol Chem 289:30842–30856. https://doi.org/10.1074/jbc.M114.574285.

10. Vitner EB, Avraham R, Achdout H, Tamir H, Agami A, Cherry L, Yahalom-Ronen Y, Politi B, Erez N, Melamed S, Paran N, Israely T. 2020. Antiviral activity of glucosylceramide synthase inhibitors against SARS-CoV-2 and other RNA virus infections. bioRxiv https://doi.org/10.1101/2020.05.18.

11. Bartke N, Hannun YA. 2009. Bioactive sphingolipids: metabolism and function. J Lipid Res 50(Suppl):S91–S96. https://doi.org/10.1194/jlr.R800080-JLR200.

12. Casasampere M, Ordoñnez YF, Pou A, Casas J. 2016. Inhibitors of dihydroceramide desaturase 1: therapeutic agents and pharmacological tools to decipher the role of dihydroceramides in cell biology. Chem Phys Lipids 197:33–44. https://doi.org/10.1016/j.chemphyslip.2015.07.025.

13. Shaner RL, Allegood JC, Park H, Wang E, Kelly S, Haynes CA, Sullards MC, Merrill AH, Jr. 2009. Quantitative analysis of sphingolipids for lipidomics using triple quadrupole and quadrupole linear ion trap mass spectrometers. J Lipid Res 50:1692–1707. https://doi.org/10.1194/jlr.D800051-JLR200.

14. Miyake Y, Kozutsumi Y, Nakamura S, Fujita T, Kawasaki T. 1995. Serine palmitoyltransferase is the primary target of a sphingosine-like immunosuppressant, ISP-1/myriocin. Biochem Biophys Res Commun 211:396–403. https://doi.org/10.1006/bbrc.1995.1827.

15. Merrill AH, van Echten G, Wang E, Sandhoff K. 1993. Fumonisin B1 inhibits sphingosine (sphinganine) N-acyltransferase and de novo sphingolipid biosynthesis in cultured neurons in situ. J Biol Chem 268:27299–27306. https://doi.org/10.1016/S0021-9258(19)74249-5.

16. Triola G, Fabriàs G, Llebaria A. 2001. Synthesis of a cyclopropene analogue of ceramide, a potent inhibitor of dihydroceramide desaturase. Angew Chem Int Ed 40:1960–1962. https://doi.org/10.1002/1521-3773(20010518)40:10<1960::AID-ANIE1960>3.0.CO;2-V.

17. Wang H, Maurer BJ, Liu YY, Wang E, Allegood JC, Kelly S, Symolon H, Liu Y, Merrill AH, Jr, Gouaze-Andersson V, Yu JY, Giuliano AE, Cabot MC. 2008. N-(4-Hydroxyphenyl) retinamide increases dihydroceramide and synergizes with dimethylsphingosine to enhance cancer cell killing. Mol Cancer Ther 7:2967–2976. https://doi.org/10.1158/1535-7163.MCT-08-0549.

18. Yasuda S, Kitagawa H, Ueno M, Ishitani H, Fukasawa M, Nishijima M, Kobayashi S, Hanada K. 2001. A novel inhibitor of ceramide trafficking from the endoplasmic reticulum to the site of sphingomyelin synthesis. J Biol Chem 276:43994–44002. https://doi.org/10.1074/jbc.M104884200.

19. Abe A, Inokuchi J, Jimbo M, Shimeno H, Nagamatsu A, Shayman JA, Radin NS. 1992. Improved inhibitors of glucosylceramide synthase. J Biochem 111:191–196. https://doi.org/10.1093/oxfordjournals.jbchem.a123736.

20. Luberto C, Hassler DF, Signorelli P, Okamoto Y, Sawai H, Boros E, Hazen-Martin DJ, Obeid LM, Hannun YA, Smith GK. 2002. Inhibition of tumor necrosis factor-induced cell death in MCF7 by a novel inhibitor of neutral sphingomyelinase. J Biol Chem 277:41128–41139. https://doi.org/10.1074/jbc.M206747200.

21. Elojeimy S, Holman DH, Liu X, El-Zawahry A, Villani M, Cheng JC, Mahdy A, Zeidan Y, Bielawska A, Hannun YA, Norris JS. 2006. New insights on the use of desipramine as an inhibitor for acid ceramidase. FEBS Lett 580:4751–4756. https://doi.org/10.1016/j.febslet.2006.07.071.

22. Draper JM, Xia Z, Smith RA, Zhuang Y, Wang W, Smith CD. 2011. Discovery and evaluation of inhibitors of human ceramidase. Mol Cancer Ther 10:2052–2061. https://doi.org/10.1158/1535-7163.MCT-11-0365.

23. French KJ, Schrecengost RS, Lee BD, Zhuang Y, Smith SN, Eberly JL, Yun JK, Smith CD. 2003. Discovery and evaluation of inhibitors of human sphingosine kinase. Cancer Res 63:5962–5969.

24. Brinkmann V, Davis MD, Heise CE, Albert R, Cottens S, Hof R, Bruns C, Prieschl E, Baumruker T, Hiestand P, Foster CA, Zollinger M, Lynch KR. 2002. The immune modulator FTY720 targets sphingosine 1-phosphate receptors. J Biol Chem 277:21453–21457. https://doi.org/10.1074/jbc.C200176200.

25. Yamamoto M, Kiso M, Sakai-Tagawa Y, Iwatsuki-Horimoto K, Imai M, Takeda M, Kinoshita N, Ohmagari N, Gohda J, Semba K, Matsuda Z, Kawaguchi Y, Kawaoka Y, Inoue J. 2020. The anticoagulant nafamostat potently inhibits SARS-CoV-2 S protein-mediated fusion in a cell fusion assay system and viral infection in vitro in a cell-type-dependent manner. Viruses 12:629. https://doi.org/10.3390/v12060629.

26. Futerman AH, Hannun YA. 2004. The complex life of simple sphingolipids. EMBO Rep 5:777–782. https://doi.org/10.1038/sj.embor.7400208.

27. Davis DL, Gable K, Suemitsu J, Dunn TM, Wattenberg BW. 2019. The ORMDL/Orm-serine palmitoyltransferase (SPT) complex is directly regulated by ceramide: reconstitution of SPT regulation in isolated membranes. J Biol Chem 294:5146–5156. https://doi.org/10.1074/jbc.RA118.007291.

28. Brown DA, Rose JK. 1992. Sorting of GPI-anchored proteins to glycolipid-enriched membrane subdomains during transport to the apical cell surface. Cell 68:533–544. https://doi.org/10.1016/0092-8674(92)90189-j.

29. Popik W, Alce TM, Au WC. 2002. Human immunodeficiency virus type 1 uses lipid raft-colocalized CD4 and chemokine receptors for productive entry into CD4(+) T cells. J Virol 76:4709–4722. https://doi.org/10.1128/jvi.76.10.4709-4722.2002.

30. Takeda M, Leser GP, Russell CJ, Lamb RA. 2003. Influenza virus hemagglutinin concentrates in lipid raft microdomains for efficient viral fusion. Proc Natl Acad Sci U S A 100:14610–14617. https://doi.org/10.1073/pnas.2235620100.

31. Vieira CR, Munoz-Olaya JM, Sot J, Jimenez-Baranda S, Izquierdo-Useros N, Abad JL, Apellaniz B, Delgado R, Martinez-Picado J, Alonso A, Casas J, Nieva JL, Fabriás G, Mañes S, Goñi FM. 2010. Dihydrosphingomyelin impairs HIV-1 infection by rigidifying liquid-ordered membrane domains. Chem Biol 17:766–775. https://doi.org/10.1016/j.chembiol.2010.05.023.

32. Uddin MG, Azam ZA. 2013. A novel oligo-DNA probe carrying non-nucleosidic silylated pyrene derivatives: synthesis and excimer forming ability. Am J Biochem Mol Biol 3:175–181.

33. Warner FJ, Lew RA, Smith AI, Lambert DW, Hooper NM, Turner AJ. 2005. Angiotensin-converting enzyme 2 (ACE2), but not ACE, is preferentially localized to the apical surface of polarized kidney cells. J Biol Chem 280:39353–39362. https://doi.org/10.1074/jbc.M508914200.

34. Li GM, Li YG, Yamate M, Li SM, Ikuta K. 2007. Lipid rafts play an important role in the early stage of severe acute respiratory syndrome-coronavirus life cycle. Microbes Infect 9:96–102. https://doi.org/10.1016/j.micinf.2006.10.015.

35. Lu Y, Liu DX, Tam JP. 2008. Lipid rafts are involved in SARS-CoV entry into Vero E6 cells. Biochem Biophys Res Commun 369:344–349. https://doi.org/10.1016/j.bbrc.2008.02.023.

36. Glende J, Schwegmann-Wessels C, Al-Falah M, Pfefferle S, Qu X, Deng H, Drosten C, Naim HY, Herrler G. 2008. Importance of cholesterol-rich membrane microdomains in the interaction of the S protein of SARS-coronavirus with the cellular receptor angiotensin-converting enzyme 2. Virology 381:215–221. https://doi.org/10.1016/j.virol.2008.08.026.

37. Finnegan CM, Rawat SS, Puri A, Wang JM, Ruscetti FW, Blumenthal R. 2004. Ceramide, a target for antiretroviral therapy. Proc Natl Acad Sci U S A 101:15452–15457. https://doi.org/10.1073/pnas.0402874101.

38. Pryor MJ, Rawlinson SM, Butcher RE, Barton CL, Waterhouse TA, Vasudevan SG, Bardin PG, Wright PJ, Jans DA, Davidson AD. 2007. Nuclear localization of dengue virus nonstructural protein 5 through its importin alpha/beta-recognized nuclear localization sequences is integral to viral infection. Traffic 8:795–807. https://doi.org/10.1111/j.1600-0854.2007.00579.x.

39. Pitts JD, Li PC, de Wispelaere M, Yang PL. 2017. Antiviral activity of N-(4-hydroxyphenyl) retinamide (4-HPR) against Zika virus. Antiviral Res 147:124–130. https://doi.org/10.1016/j.antiviral.2017.10.014.

40. Makena MR, Koneru B, Nguyen TH, Kang MH, Reynolds CP. 2017. Reactive oxygen species-mediated synergism of fenretinide and romidepsin in preclinical models of T-cell lymphoid malignancies. Mol Cancer Ther 16:649–661. https://doi.org/10.1158/1535-7163.MCT-16-0749.

41. Hong JH, Kim MJ, Park MR, Kwag OG, Lee IS, Byun BH, Lee SC, Lee KB, Rhee SJ. 2004. Effects of vitamin E on oxidative stress and membrane fluidity in brain of streptozotocin-induced diabetic rats. Clin Chim Acta 340:107–115. https://doi.org/10.1016/j.cccn.2003.10.003.

42. Maurer BJ, Kang MH, Villablanca JG, Janeba J, Groshen S, Matthay KK, Sondel PM, Maris JM, Jackson HA, Goodarzian F, Shimada H, Czarnecki S, Hasenauer B, Reynolds CP, Marachelian A. 2013. Phase I trial of fenretinide delivered orally in a novel organized lipid complex in patients with relapsed/refractory neuroblastoma: a report from the New Approaches to Neuroblastoma Therapy (NANT) consortium. Pediatr Blood Cancer 60:1801–1808. https://doi.org/10.1002/pbc.24643.

43. Veronesi U, Mariani L, Decensi A, Formelli F, Camerini T, Miceli R, Mauro MGD, Costa A, Marubini E, Sporn MB, Palo GD. 2006. Fifteen-year results of a randomized phase III trial of fenretinide to prevent second breast cancer. Ann Oncol 17:1065–1071. https://doi.org/10.1093/annonc/mdl047.

44. Villablanca JG, Krailo MD, Ames MM, Reid JM, Reaman GH, Reynolds CP. 2006. Phase I trial of oral fenretinide in children with high-risk solid tumors: a report from the Children's Oncology Group (CCG 09709). J Clin Oncol 24:3423–3430. https://doi.org/10.1200/JCO.2005.03.9271.

45. Mody N, McIlroy GD. 2014. The mechanisms of fenretinide-mediated anticancer activity and prevention of obesity and type-2 diabetes. Biochem Pharmacol 91:277–286. https://doi.org/10.1016/j.bcp.2014.07.012.

46. Orienti I, Gentilomi GA, Farruggia G. 2020. Pulmonary delivery of fenretinide: a possible adjuvant treatment in COVID-19. Int J Mol Sci 21:3812. https://doi.org/10.3390/ijms21113812.

47. Matsuyama S, Nao N, Shirato K, Kawase M, Saito S, Takayama I, Nagata N, Sekizuka T, Katoh H, Kato F, Sakata M, Tahara M, Kutsuna S, Ohmagari N, Kuroda M, Suzuki T, Kageyama T, Takeda M. 2020. Enhanced isolation of SARS-CoV-2 by TMPRSS2-expressing cells. Proc Natl Acad Sci U S A 117:7001–7003. https://doi.org/10.1073/pnas.2002589117.

48. Bligh EG, Dyer WJ. 1959. A rapid method of total lipid extraction and purification. Can J Biochem Physiol 37:911–917. https://doi.org/10.1139/o59-099.

49. Hama K, Fujiwara Y, Tabata H, Takahashi H, Yokoyama K. 2017. Comprehensive quantitation using two stable isotopically labeled species and direct detection of N-acyl moiety of sphingomyelin. Lipids 52:789–799. https://doi.org/10.1007/s11745-017-4279-5.

50. Ishibashi Y, Ito M, Hirabayashi Y. 2018. Regulation of glucosylceramide synthesis by Golgi-localized phosphoinositide. Biochem Biophys Res Commun 499:1011–1018. https://doi.org/10.1016/j.bbrc.2018.04.039.

51. Yuyama K, Sekino-Suzuki N, Sanai Y, Kasahara K. 2007. Translocation of activated heterotrimeric G protein Gαo to ganglioside-enriched detergent-resistant membrane rafts in developing cerebellum. J Biol Chem 282:26392–26400. https://doi.org/10.1074/jbc.M705046200.

52. Yan G, Wang H, Luna A, Bozorgui B, Li X, Sanchez M, Dereli Z, Kahraman N, Kara G, Chen X, Lu Y, Babur O, Cokol M, Ozpolat B, Sander C, Mills GB, Korkut A. 2020. Adaptive response to BET inhibition induces therapeutic vulnerability to MCL1 inhibitors in breast cancer. bioRxiv https://doi.org/10.1101/711895.